Dosimetric verification of murine proton irradiations and in vitro analysis of DNA damage repair modulators and FLASH irradiations

Master Thesis

Eva van Oosten

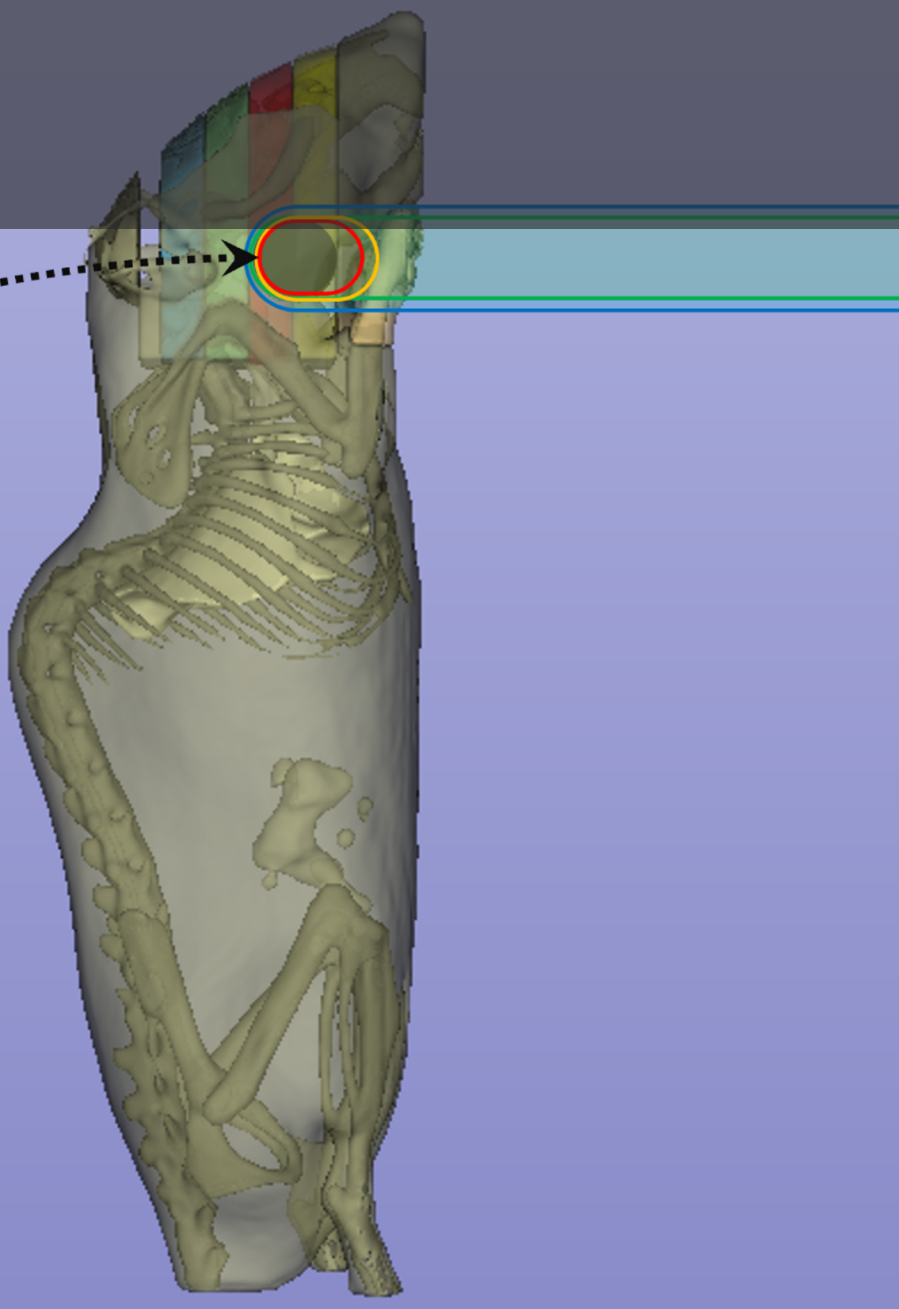

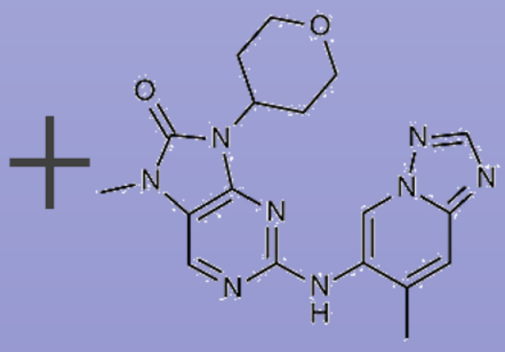

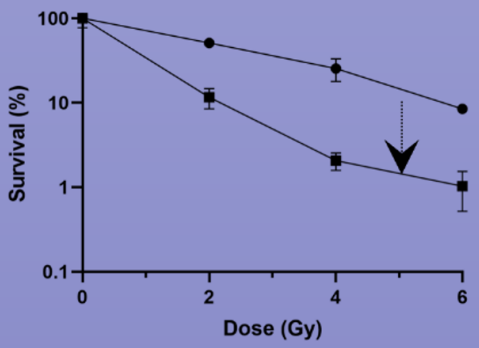

Erasmus MC
HollandPTC
Protonen Therapie Centrum

Dosimetric verification of murine proton irradiations and in vitro analysis of DNA damage repair modulators and FLASH irradiations

Master Thesis

by

Eva van Oosten

to obtain the degrees of

Master of Science in Nanobiology and Biomedical Engineering

at the Molecular Genetics and Radiotherapy departments of Erasmus Medical Center
to be defended publicly on November 1st 2022, at 14:30.

Student number:	4571401
Supervisors:	Dr. Jeroen Essers and Prof. Dr. Mischa Hoogeman
Daily supervisors:	Tim Heemskerk and Dr. Steven Habraken
External committee members:	Dr. Alex Zelensky and Dr. ir. Dennis Schaart
Institution:	Erasmus Medical Center
Project Duration:	September 2021 - November 2022

Erasmus MC

HollandPTC
Protonen Therapie Centrum

Preface

More than a year ago I started this thesis project to finish my Master programs Nanobiology and Biomedical Engineering. After lots of ups and downs, I am happy with the result that you are holding right now. I am very grateful for everyone involved in the project and supporting me. To me, this thesis really feels like a major group effort and I am really glad I could have been part in this.

I would like to thank my supervisors Mischa Hoogeman, Jeroen Essers, Steven Habraken, and Tim Heemskerk for your guidance and coaching during the project and biweekly meetings. Tim, thank you for teaching me the laboratory techniques, for your quick and useful feedback on thesis pieces, and for the many conversations we had. I admire your work-life balance and how experimental difficulties do not impact yourself at all. It is an essential skill and I hope to learn that myself as well. Steven, thank you for all our discussions on the thesis and literature review. I have learned a lot from you about proton therapy, CTs, research and the clinic in general, and myself. Jeroen, thank you for your guidance, for keeping an eye on the bigger picture, for your feedback on the thesis, and for a very meaningful conversation in the train. And Mischa, I would like to thank you for your constructive feedback during the meetings and for coaching me in this project.

The 1st of November, Dennis Schaart and Alex Zelensky will join as members of the thesis committee. I am grateful that you are willing to be part of this and I look forward to our discussion.

Repeating X-ray experiments with protons is difficult due to its sophisticated set-up, but Marta Rovituso, Wouter van Burik, and Soraya Naït Abdellah made this possible. Thank you for assisting in all proton irradiations. Marta, together with Ernst van der Wal we worked on the murinemorphic phantom and its irradiation. I am grateful to you two for our collaboration in this. Ernst, you made a wonderful 3D-printed mouse and I really enjoyed the written explanations you left in the research bunker.

The CT scans were performed with Yanto Ridwan, Joost Haeck, and Sandra van Tiel. I would like to thank you for scanning the inserts and phantom with me and for explaining everything. Together with Monique Bernsen and Jeroen Essers, we have had interesting discussions on improvements of the CT scanning procedure. Thank you.

Of course, I would not forget the combined Radiobiology group. I appreciate the meetings we had, your help with laboratory experiments, and our group outings. Besides this, the atmosphere in the office has been good all year long. Thank you to all of the current and previous office members.

I really enjoy that Michèle Knol is currently continuing on the CT calibration. Michèle, our discussions were very valuable and I wish you the best of luck with your project. I look forward to seeing your results.

At last I would like to show my gratitude to the people closest to me. Gian, thank you for showing me that developing yourself outside of studies is fun and important. During our ballroom sessions, my mind could finally be freed from the thesis. And dear family and friends, the pandemic has teached me how important you are to me. Thank you for keeping me sane during this year and for all the lovely get-togethers. I am determined to stay in this area to stay physically close to you. Yet even if our paths separate us physically, I know we will keep contact.

Eva van Oosten
Delft, October 2022

Abstract

With almost 900.000 new patients per year suffering from head and neck squamous cell carcinomas (HNSCC), who after radiotherapy treatments experience severe side effects, the focus is drawn to proton therapy. Proton therapy results to less side effects since healthy tissues surrounding the tumour receive less radiation dose. This results from the proton's specific depth-dose profile with its Bragg peak.

To further reduce the effect on surrounding tissues, major improvements should be made in understanding the biologic response to proton therapy which will eventually lead to enlarging the therapeutic window. Here in vitro analysis with DNA damage repair inhibition or increasing proton dose rates can be performed to assess which DNA repair pathways repair radiation induced DNA damage and to assess the effect of proton dose rates on biological tissues. This will be investigated in vitro, while in vivo experiments are necessary as well. However, currently most mice are irradiated with protons in the plateau of the Bragg curve instead of the Bragg peak. Therefore, a dosimetric pipeline should be designed to allow for accurate placement of mouse tumours in the proton's Bragg peak.

In this thesis, the osteosarcoma- and HNSCC-derived U2OS and FaDu cell lines were incubated with non-homologous end-joining or homologous recombination inhibitors during x-ray and proton irradiations. We have shown a radiosensitising effect of the non-homologous end-joining inhibitor AZD7648 on FaDu cells during x-ray irradiation, but an effect during proton irradiation could not be proved nor neglected. The homologous recombination inhibitor B02 could not effectively inhibit homologous recombination and was shown to not affect clonogenic survival of FaDu during X-ray irradiations. The observed radiosensitising effect of the non-homologous recombination inhibitor AZD7648 can be exploited in patient selection based on already existing DNA damage repair deficiencies in the tumour. Furthermore, combination therapies could be used of photon irradiations with AZD7648 targeted to the tumour to artificially enlarge the therapeutic window.

Besides this, the HNSCC-derived FaDu cells were irradiated with varying dose rates to assess induction of a FLASH effect. This FLASH effect is usually observed after irradiations of $>$40 Gy/s resulting in a reduction of normal tissue complications while tumour control is maintained. In our analysis, small differences in low dose rates did not have any impact. The experimental set up for proton FLASH irradiations of cells was prepared and though we performed the first set of experiments no definite conclusion could be drawn due to the level of biological variation we observed.

Of course, differential effects between tumours and tissues like the FLASH effect should be investigated in vivo. Therefore, a set-up should be created to irradiate the mural tumour with Bragg peak protons. To reach this, two micro-CT scanners were calibrated to link Hounsfield units to stopping power ratios. The proton range in mice was determined and a 3D-printed mouse-like phantom was irradiated. In this thesis, determined stopping powers of all CIRS phantom inserts except for lung tissues were accurate with a maximum deviation of 2% or 6.5% after calibration with QuantumGx or VECTor micro-CT scanners. Larger deviations were observed for CIRS lung inserts or Gammex inserts. The irradiated gafchromic films inserted in the murinemorphic phantom showed dose distributions visualising the mouse's anatomy, yet the dose was too low due to irradiation in the distal edge of the Bragg peak. The latter was confirmed with Monte Carlo simulations. This dosimetric set-up to place mice tumours in the proton Bragg peak should thus be slightly improved and can then be of great value for in vivo experiments of proton therapy. This enables execution of many new experiments with DNA damage repair inhibition and FLASH irradiations, potentially leading to an increase of the therapeutic window in proton therapy and less side effects for HNSCC-patients.

Contents

Nomenclature

Abbreviation	Full term
3D	Three-dimensional
AMIE	Applied Molecular Imaging Erasmus MC
BSA	Bovine serum albumin
CDD	Complex DNA damage
CT	Computed tomography
DDR	DNA damage response
DMSO	Dimethyl sulfoxide
DNA	Deoxyribonucleic acid
DSB	Double-stranded break
Erasmus MC	Erasmus Medical Center
FCS	Fetal calf serum
GFP	Green fluorescent protein
HIPS	High impact polystyrene
HNSCC	Head and neck squamous cell carcinoma
Holland PTC	Holland Proton Therapy Center
HR	Homologous recombination
HU	Hounsfield unit
ICRP	International Commission on Radiological Protection
LET	Linear energy transfer
NHEJ	Non-homologous end-joining
OAR	Organ at risk
p-Ser2056 DNA-PKcs	DNA-PKcs phosphorylated on serine 2056
PBS	Phosphate buffered saline
PLA	Polylactide
PTV	Planning target volume
RBE	Radiobiological effectiveness
RSP	Relative stopping power
SDS	Sodium dodecyl sulfate
SOBP	Spread-out Bragg peak
SPR	Stopping power ratio
ssDNA	Single-stranded DNA
WET	Water-equivalent thickness

Note: FLASH is not an abbreviation.

List of Figures

List of Tables

1 Introduction

In 2020 there were almost 900.000 new patients with head and neck cancer [1]. This cancer type originates in the squamous cell linings of the mouth and throat and is thus called head and neck squamous cell carcinomas (HNSCC) [2]. Often, these cancers are treated using photon radiotherapy, which results in various side effects like a dry mouth, difficulties in swallowing, necrosis of bone cells, problems in chewing, and hearing loss. These side effects are caused by irradiation of the glands, muscles, bones, joints, and inner ear in the head and neck region [3] which are in close proximity of the primary tumor and are thus difficult to avoid.

1.1. Proton therapy

Proton radiotherapy succeeds better in treating the tumour region while sparing the surrounding healthy tissues than photon therapy. This results from the proton's dose deposition, which starts moderately at the entrance plateau, increases until reaching the Bragg Peak and falls off rapidly behind (Fig. 1.1a). This Bragg curve originates from the interactions of protons with material leading to a decrease in proton energy. The lower the proton's energy, the stronger the stopping power of the material. Therefore, protons lose energy faster and faster while traversing media until their energy reaches 0 eV. This results in the strong energy deposition of the protons in the Bragg peak region.

The larger the proton beam's energy at the start, the further the protons can travel before losing all their energy. The proton's energy thus correlates with their range. Besides this, the denser the material the protons interact with, the shorter their range.

The pristine Bragg peak is however not used much in treatments, since its small region of homogeneous dose leads to difficult homogeneous irradiations of tumours. Therefore, usually the spread-out Bragg peak is used for treatments. This broader Bragg peak is created by summing multiple Bragg peaks with varying energies and thus varying depths (Fig. 1.1b).

Due to the SOBP, organs at risk (OARs) positioned distal of the tumour are successfully avoided. Plan comparison for 45 HNSCC patients between photon and proton therapy showed a reduced dose deposition to the OARs and reduced normal tissue complication probability for proton therapy for all patients [5]. This effect is most pronounced for OARs (partly) outside of the planning target volume (PTV).

Biological tissues respond differently to protons with respect to photons, which is described by the radiobiological effectiveness (RBE). This RBE is the division of the dose necessary in proton irradiations to yield the same effect as photons with the dose used for photon irradiations, which was thought to be 1.1. However, it was shown that the RBE is correlated with the amount of energy deposited per distance traveled (linear energy transfer (LET)) [6]. Since the LET of protons varies through the Bragg curve, the RBE changes over depth as well. The LET in the Bragg peak is approximately six times as high as the LET in the plateau, leading to an increase of 15% in RBE [7].

On a molecular level, the secondary electrons emerging from proton irradiations either directly hit the DNA leading to DNA damage or hit surrounding water molecules. This creates radicals and ions which will in turn damage the DNA. These ionisations take place instantaneously. It is widely accepted that photon therapy leads to base damage, single and double strand breaks, while proton therapy

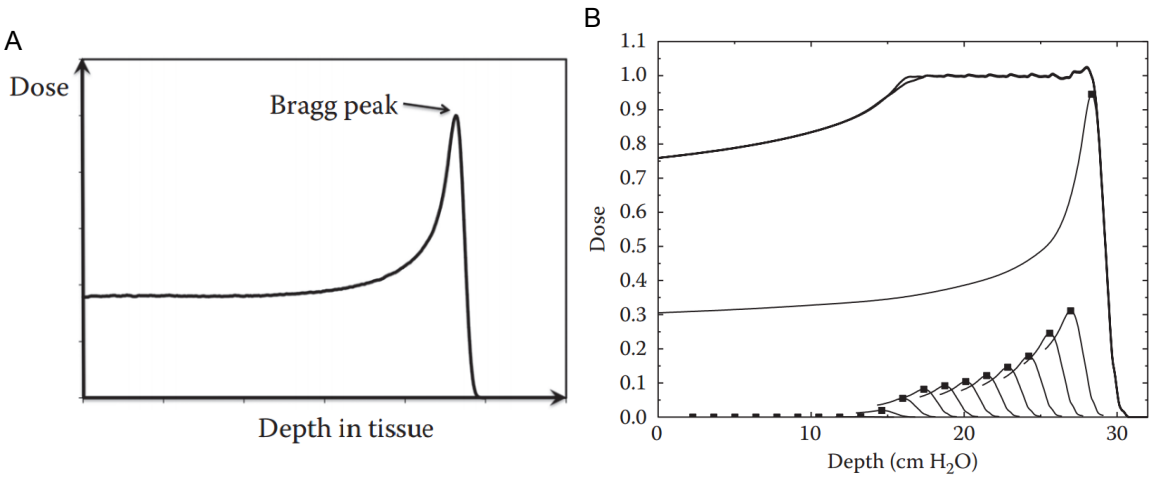

Figure 1.1: **The depth-dose curve for proton irradiations.** (A) Single energy proton beams lose energy while interacting with traversed tissues. This effect is stronger for low energy protons, leading to strong energy deposition in the Bragg peak. (B) Summing multiple single energy proton beams leads to a broader depth-dose curve with a spread-out Bragg peak. Figures retrieved from [4].

induces more clustered complex DNA damage (CDD) in the Bragg peak's distal edge, which results from the high LET in the Bragg peak's distal edge.

1.2. Cellular response to radiation

Irradiations induce DNA damage, which may lead to apoptosis when not repaired correctly. Several studies suggest that simple photon-induced damage is repaired by non-homologous end-joining while the clustered complex DNA damage induced by protons requires homologous recombination [8–10]. Yet clear evidence is not available yet.

Radiation-induced double stranded breaks are first detected by a complex of Mre11, Rad50, and Nbs1. Together with Rad50 and Nbs1, the endonuclease Mre11 will resect the ends of the double-stranded breaks leading to small overhangs. This generally induces non-homologous end-joining to repair the damage. Larger resections may be created by the nucleases Exo1 and DNA2, which induces the execution of homologous recombination [11].

During non-homologous end-joining (NHEJ) both sides of a double-stranded break are detected and ligated (Fig.1.2). First, the Ku70/Ku80 heterodimer detects the dsDNA ends, interacts with its backbone, and recruits DNA-PKcs. This enzyme constantly binds and unbinds the DNA until it is autophosphorylated. Only then, DNA-PKcs can recruit downstream proteins [12]. The small DNA overhangs cannot be repaired directly and are thus processed by artemis and DNA polymerases. Finally, the DNA ends are ligated by the dimer DNA ligase IV/XRCC4 [13]. Non-homologous end-joining rapidly repairs the DNA damage avoiding harmful structural rearrangements and induction of apoptosis. However, due to the ligation, not all DNA bases may be restored and a small deletion can be induced.

A deletion will not appear after DNA damage repair using homologous recombination (HR). This DNA repair pathway functions inherently different by resection, the search of homologous DNA, and DNA synthesis (Fig.1.2). First, the overhangs are resected on which RPA is bound. BRCA2 inhibits binding of RPA to the resected DNA strand allowing Rad51 to bind. Rad51 creates helical filaments which enables recruitment of downstream proteins [14]. Rad54 and the Rad51 filament interact such that the filament opens double stranded DNA and Rad54 can detect homologous sequences in the separated DNA strands [15]. Once homologous DNA has been detected, Rad54 further guides the formation of the heteroduplex DNA of the damaged and donor DNA. DNA polymerase binds to this complex and DNA synthesis takes place.

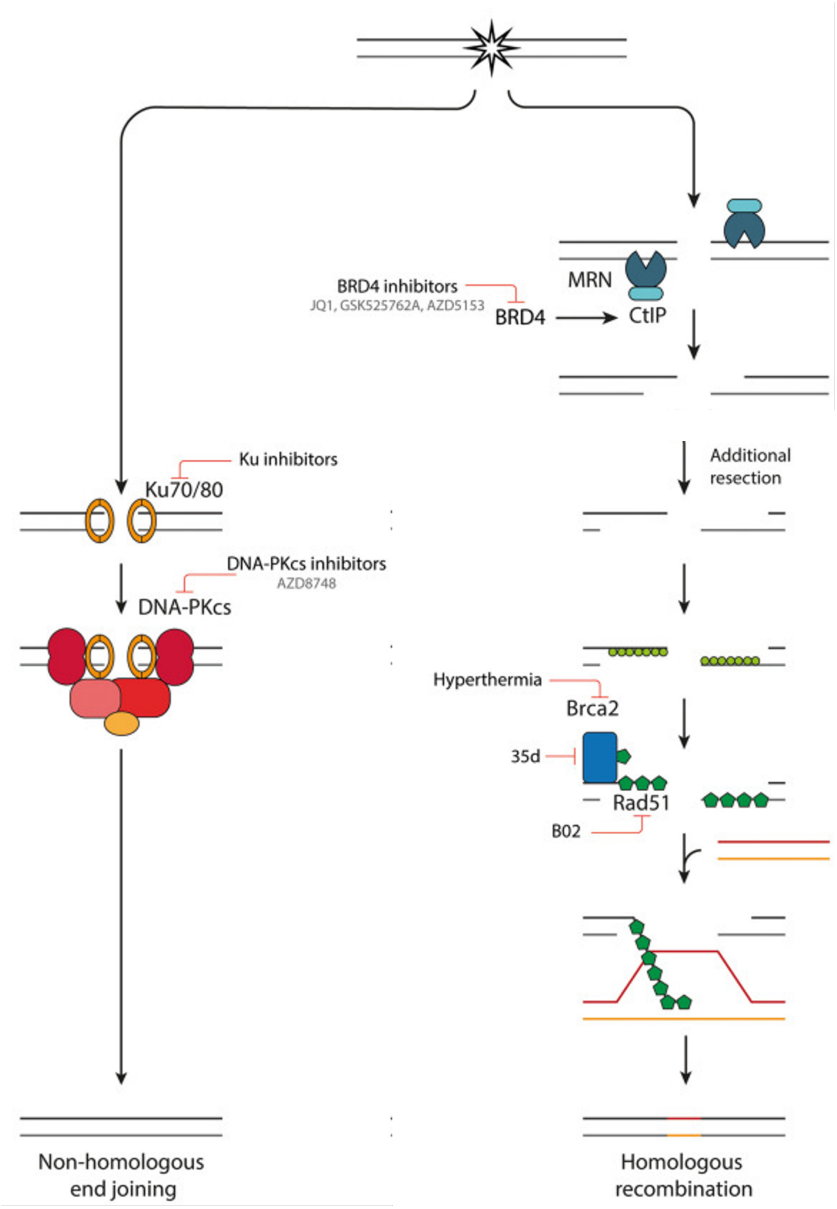

Figure 1.2: **DNA damage reparation by non-homologous end-joining and homologous recombination.** Small molecule inhibitors AZD7648 and B02 block DNA damage repair by inhibition of DNA-PKcs autophosphorylation or binding of Rad51 to the DNA. Figure adjusted from [16].

Unraveling which DNA damage repair pathway is used after photon and proton irradiations, can be performed by inhibition of a single pathway. The small-molecule inhibitor AZD7648 inhibits the autophosphorylation of DNA-PKcs [17]. If DNA-PKcs is not phosphorylated on Ser2056, the DNA ends are not exposed inhibiting binding of the downstream proteins to the DNA. Therefore the DNA overhangs can not be processed nor ligated [12]. The small molecule inhibitor B02 inhibits homologous recombination by preventing binding of Rad51 to the DNA [18]. Therefore, no filament is created which together with Rad54 would find the homologous DNA. Without a donor template, there is no template for DNA synthesis and thus the double-stranded break cannot be repaired.

In this thesis, the small-molecule inhibitors AZD7648 and B02 will be supplemented to cells during photon or proton irradiation. Comparing clonogenic survival after the irradiation may provide knowledge on the type of DNA repair pathway required to repair radiation-induced DNA damage after different types of irradiation.

1.3. Dosimetry for proton therapy

Ideally, the spread-out Bragg peak is shifted such that it overlays the tumour, leading to a homogeneous dose in the tumour and only minor doses to the surrounding healthy organs-at-risk (OARs). The position of the SOBP, the proton beam's range, depends on the initial energy spectrum of the protons ans the stopping power ratios of the tissues traveled through. The stopping power is the energy loss of protons per unit path length through a specific tissue and is often expressed relative to water. Oversimplified, the stopping power of denser tissues is larger than from less dense tissues, yet the exact anatomical composition plays a role as well. This is expressed in the Bethe-Bloch formula as

$$RSP = \frac{\rho N_g}{\rho_{\text{water}} N_{g,\text{water}}} \frac{ln\frac{2m_e c^2 \beta^2}{I_m(1-\beta^2)} - \beta^2}{ln\frac{2m_e c^2 \beta^2}{I_{\text{water}}(1-\beta^2)} - \beta^2} \tag{1.1}$$

in which ρ is the density, m_e the mass of an electron, c the speed of light, $\beta = \frac{v_{\text{proton}}}{c}$ the relative proton velocity with respect to the speed of light, $N_g = N_A \Sigma \frac{w_i Z_i}{A_i}$ the number of electrons per unit volume determined from the weight, atomic numbers, and atomic mass of all included atoms, and I the ionisation energy. The latter is summed for all atoms within a molecule via the Bragg additivity rule as

$$ln(I_m) = (\Sigma \frac{w_i Z_i}{A_i} ln(I_i))/(\frac{w_i Z_i}{A_i}) \tag{1.2}$$

in which the ionisation energy per atom approximates 19.0 eV for hydrogen, 11.2+11.7·Z eV for elements with atomic numbers until 13, and 52.8+8.71·Z eV for elements of atomic number exceeding 13 [19]. With this, the stopping power of each biological tissue can be determined. Knowledge of the relative stopping power of the tissues in the irradiated field is necessary to accurately determine the range of the protons.

Usually before the treatment, a Computed Tomography (CT) scan is performed to visualise the tumour and the inhomogeneities in surrounding tissues. During CT scans, X-rays are targeted towards a detector and interact with tissues they travel through. During these interactions, X-rays are attenuated leading to a drop in signal at the detector. This attenuation coefficient depends the density of the material, its atomic number, and the photon's energy. The x-ray tube generates polychromatic X-rays, which due to their varying energies are attenuated differently. The strong attenuation of low energy photons results in a shift to a higher average energy. Therefore, at highers depths, the average energy is high, leading to less attenuation than expected from the tissue properties alone. This results in so-called beam-hardening artefacts, dark spots in the image, which can be removed physically by the addition of an aluminium filter behind the x-ray tube eliminating the lowest energy photons from the beam already [20].

To create a three-dimensional image, many projection images are made from various angles by rotating the detector and source around the object (Fig. 1.3a). Reconstruction towards a three-dimensional image from the projection is performed via filtered backprojection [21]. The projections made are first combined in backprojection (Fig. 1.3b). The measured intensities of a single projection image are assigned to all voxels on the line from the source to the detector. This is performed for all projection images and summed. The point-like object from figure 1.3a is recognised clearly when summing multiple backprojected projection images. The poor resolution of the point-like object is improved by convolving all projection images with a sharp kernel. Together these methods are known as filtered backprojection.

From the CT scans, information about the electron densities of the object's materials is assessed instead of the density and atomical composition necessary for stopping power predictions. A calibration should convert the measured Hounsfield Units (HU) to proton stopping power ratios from which the range can be calculated. It has been shown that the use of a stoichiometric calibration of the CT scanner used for patient dose planning in combination with Monte Carlo simulations succeeds in this conversion and decreases the range uncertainty to less than 0.5 mm [23]. In general, stoichiometric Ct calibrations link HU values to tissue properties and determine the stopping power ratio from this information. Assessment of CT calibration methods of various proton therapy institutes, showed that stoichiometric methods resulted in accurate stopping power estimates as well [24]. These however,

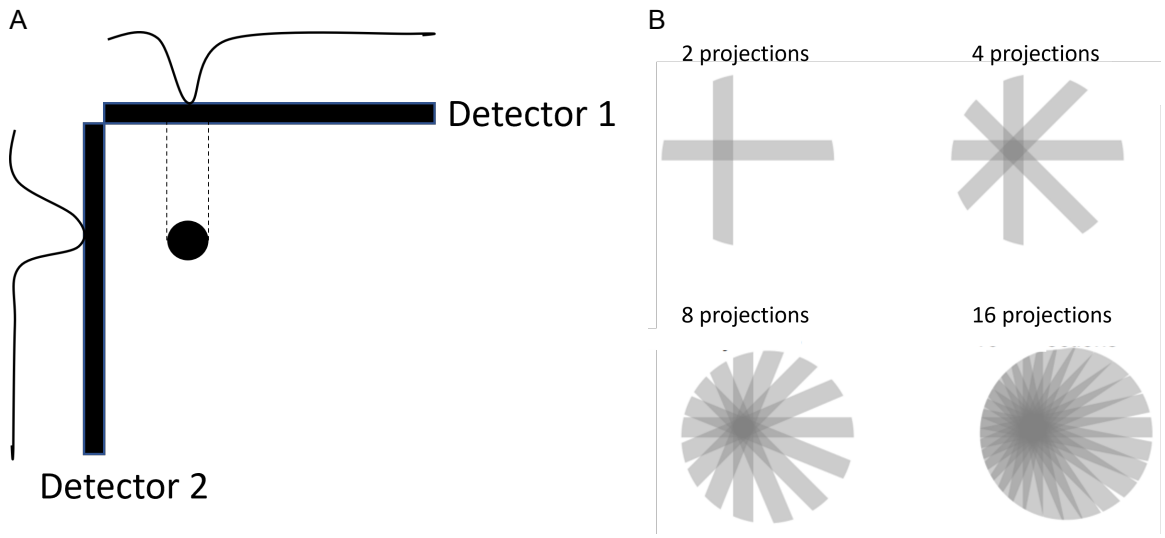

Figure 1.3: **Schematic overview of backprojection.** (A) Projection images are collected from a point-like object. (B) Projections are backprojected and summed resulting in detection of the point-like object when many projections are used. Figure adjusted from [22].

had all been performed on clinical CT scanners.

In this thesis, a stoichiometric calibration will be executed for micro-CT scanners used for small-animal visualisation. In this calibration, HU values will be mapped to proton stopping powers using the elemental composition of biological tissues. This will be performed for two different micro-CT scanners to also assess the robustness of the method. Validation will be performed by calculation of the stopping power ratios from known material properties, and by irradiation of a 3D-printed phantom resembling mice in geometry and materials from which the final calculated proton range can be checked.

1.4. The FLASH effect

Ultra-high dose rate irradiations were shown to induce less healthy tissue complications in the 1960's by various studies [25]. No further research was performed on these irradiations until Favaudon et al. confirmed the decrease of healthy tissue complications for lung tumour bearing mice [26]. Yet, there most striking finding was that their lung tumour bearing mice showed less lung fibrosis while the same tumour control was reached as with lower dose rates. This differential effect between healthy and cancerous tissues was a breakthrough and was called the FLASH effect.

Even though the initial ultra-high dose rate experiments were performed with photons, this differential FLASH effect has also been shown using protons. FLASH irradiations make use of ultra-high dose rates of >40 Gy/s. It has been widely shown in mice that healthy tissue complications are decreased while tumour control is maintained [27, 28]. The mammary carcinoma carrying mouse hind limbs of Sørensen et al. for example experienced less radiation induced fibrosis and skin damage when treated with ultra-high instead of conventional dose rates. The FLASH effect has even been observed for ultra-high dose rate irradiations of higher animal models like mini-pigs and cats [29]. Yet these FLASH irradiations were performed with electrons. The first patient has already been treated with FLASH radiotherapy [30]. The patient had a lymphoma which had disseminated over a large skin surface. The skin tumour was irradiated with 15 Gy with FLASH electrons and surrounding tissues were examined regularly. The tumour shrunk rapidly and there was only limited effect on the surrounding healthy skin. Due to this successful treatment, the first clinical trial started in 2020 [31]. This single armed feasibility study includes ten patients with symptomatic bone metastases in the extremities. The results will be published at the end of 2022.

Even though the FLASH effect has been shown multiple times in vivo and in a patient, the underlying mechanism is still unknown. Hypotheses range from the effect of oxygen depletion and Reactive Oxygen Species to the role of the immune system. Some suggest that the fast irradiation leads to oxygen

depletion. It was shown that irradiations leading to a FLASH effect would not succeed anymore at doubled oxygen concentrations [32]. Since irradiated oxygen splits into radicals which damage the DNA, the oxygen concentration is indeed relevant for radiotherapy. Others confirm the oxygen depletion during FLASH radiotherapy, yet quantitatively show that this drop is too small to explain the FLASH effect alone [33]. Another hypothesis is that the immune system plays a role in the FLASH effect. During the first in vivo FLASH experiments TGF-β signalling decreased [26]. Later studies confirmed this decreased level of this immune response regulator called TGF-β for in vitro studies. Besides, decreased expression of TGB-β, the immune system may affect the response to FLASH irradiations via different routes as well. The levels of macrophages and T lymphocytes seem to differ for FLASH treatments, but evidence is still missing. Besides this, it has been suggested that during the ultra-fast FLASH irradiations less circulating immune cells are hit, resulting in a less compromised immune system.

For investigation of biological mechanism many in vitro experiments can be designed. However, even though ultra-high dose rate irradiations lead to a FLASH effect in vivo, in vitro ultra-high dose rate proton experiments have not yet led to clear evidence for the presence of a FLASH effect. In this thesis, we will execute ultra-high dose rate proton irradiations on head and neck cancer cells to assess the presence of a FLASH effect in vitro for this specific cell line.

1.5. Research questions

The overarching goal is improvement of proton therapy focused on the reduction of side effects for patients by enlarging the therapeutic window. In this thesis, three subjects were investigated contributing to this goal (Fig. 1.4).

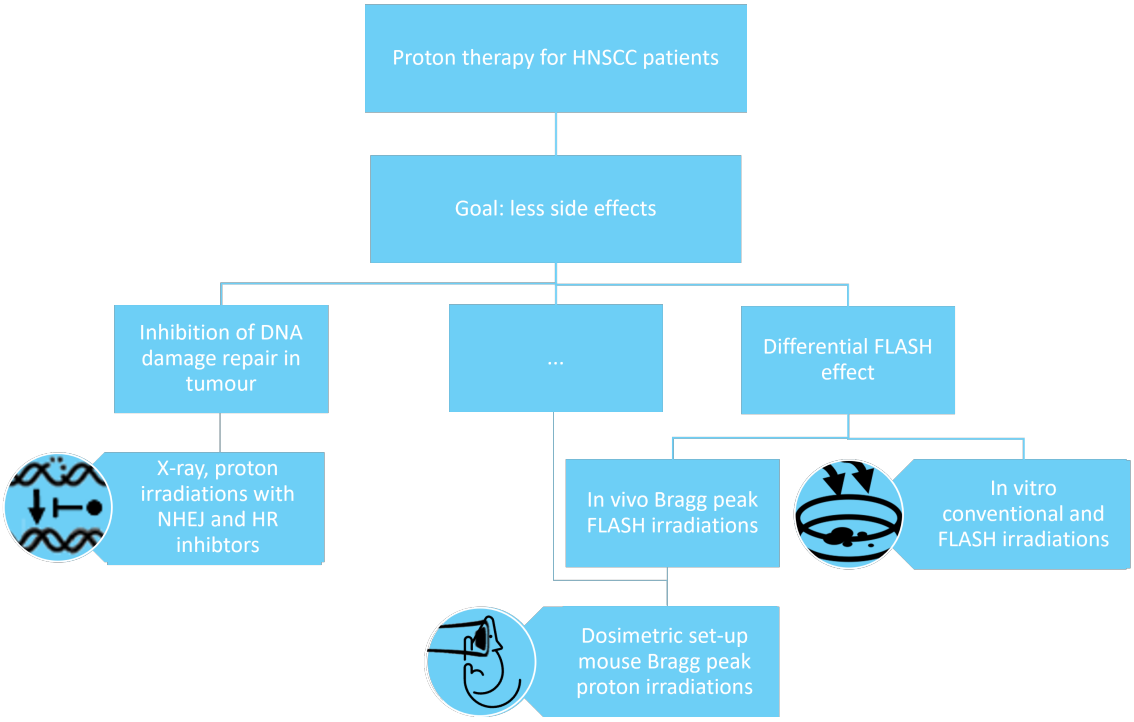

Figure 1.4: **Schematic diagram of this thesis contributing to less side effect for HNSCC patients.** In this thesis, three subjects were investigated which all help to improve proton therapy for head and neck patients.

The type of DNA damage and subsequent DNA damage repair may be influenced by the type of radiation the damage is induced by. Therefore, we investigate the effect of DNA damage repair inhibitors on cells irradiated with photons and protons. Observed radiosensitisation of cells by DDR inhibitors during a certain type of radiation, suggests that this radiation type induces damage which can be repaired by the inhibited DNA damage repair pathway. The main research question and its subquestions we focus on are:

➤ Which DNA damage repair inhibitors radiosensitise U2OS and FaDu cell lines during photon and proton irradiations?

- How does the non-homologous end-joining inhibitor AZD7648 affect clonogenic survival of FaDu after x-ray and proton irradiations?
- How does the homologous recombination inhibitor B02 affect clonogenic survival of FaDu after x-ray and proton irradiations?

Next to acquiring fundamental knowledge on DNA damage repair after different types of radiation, answering these questions may in the future be used in patient selection. Whenever patients carry DDR mutations in their tumours, the radiation type could be selected which induces damage which need to be repaired by the repair pathway the tumour has deficiencies in. This would further enlarge the therapeutic window. Besides this, the small-molecule inhibitors may be used in combination therapies of DNA damage repair inhibitors with radiation.

Differential effects like the FLASH effect between tumours and tissues can only be investigated in vivo. Here, the tumour should be irradiated with Bragg peak protons to mimic the clinical set-up as much as possible. Therefore, accurate dosimetry of Bragg peak irradiations in mice should be carried out. Accurate positioning of the Bragg peak is especially difficult due to the small dimensions of mice allowing for much smaller deviations in proton range. The following research question and subquestions will be addressed:

➤ What dosimetric verification results in accurate Bragg peak irradiations of artificial mouse head and neck cancer patients?

- How are micro-CT scanners calibrated for proton stopping power ratio predictions?
- What experimental dosimetric pipeline allows for proton range validation in mice?
- Can Monte Carlo simulations further validate range estimation?

Accurate positioning of the Bragg peak in mice would enable execution of many in vivo experiments dependent on comparisons of healthy and tumour tissue and would therefore highly boost research on proton therapy.

For now, an attempt to induce the FLASH effect in vitro will already be made. Here, the following research question will be answered:

➤ Do ultra-high dose rate proton irradiations induce a FLASH effect in the head and neck cancer cell line FaDu?

The induction of the FLASH effect in vitro will enable many research experiments on the biological mechanism of FLASH. Insights into the biological mechanism of FLASH will be important to ethically validate clinical trials or actual treatments of patients with ultra-high dose rates.

1.6. Structure of the thesis

The methods used in this thesis are discussed in chapter 2. From these experiments results were generated as described in chapter 3. A discussion of the results, their assumptions, shortcomings, and implications can be found in chapter 4 in which recommendations for further research are reported as well. At last, conclusions are drawn from this thesis in chapter 5.

2

Methods

2.1. Radiosensitisation by DNA damage repair inhibition

2.1.1. Cell culture

Human epithelial U2OS cells were cultured in Dulbecco's modified Eagle's medium (Gibco 41966-029) with 10% fetal bovine serum and 1% penicillin-streptomycin (Sigma-Aldrich P0781). The head and neck squamous cell carcinoma-derived cell line FaDu was cultured in an equal volume mixture of Dulbecco's modified Eagle's medium and Ham's F10 (Biowest L0140) with 10% fetal bovine serum and 1% penicillin-streptomycin. Both cell lines were split twice a week by washing them with Phosphate Buffered Saline (PBS, Lonza Biowhittake BE17-512F), incubating them 5 minutes in a trypsin/EDTA (Sigma-Aldrich T3924) solution to detach, and transferring a sixth to the next plate. The cells were maintained at 37°C and 5% CO2.

2.1.2. Cell irradiations

Clonogenic survival after X-ray irradiation

Cells were trypsinised and counted using an automated cell counter (Countess II, InVitrogen). Cells were seeded in 6 cm dishes in triplicates with U2OS concentrations of 200, 400, 800, 1600 cells/dish and FaDu concentrations of 300, 600, 1200, 2400 cells/dish for the irradiations of 0, 2, 4, 6 Gy respectively. Cells were allowed to attach to the dish for 8 hours after which they were irradiated with 195 kV X-rays (10 mA, 0.5 mm Cu filter) at 300 mm from the source in the RS320 (Xstrahl) X-ray irradiation cabinet.

Colonies were allowed to form for 7 and 14 days for U2OS and FaDu respectively. The cells were stained after 7 days and 14 days respectively by removing the medium, washing with PBS, incubating for 30 minutes in Coomassie Blue (25% methanol, 0.5% acetic acid, and 0.5 g 0.1% brilliant blue R in demi water), and rinsing and drying in air. Colonies were then counted with the Gelcount colony counter (Oxford optronix).

Clonogenic survival after proton irradiation

Before irradiating, Dosimetry was performed by doing two irradiations with 150 MeV protons for 10 seconds and counts were measured by the Markus chamber (PTW). Together with the measured atmospheric pressure and temperature, the dose rate could be determined.

Cells were seeded in T25 flasks (Greiner Bio-one, 690160) with 2.5 million cells in 4 mL the day before the irradiation to adhere and form a monolayer. The cells were put in a custom made system to flip flasks upright (flipper system made by DEMO (Delft)) and were flipped vertically just before irradiation. For the irradiations, 150 MeV proton were used at a beam current of 800 nA. Cells were irradiated in a 10x10 cm homogeneous field created by the beamline as shown in figure 2.1 (specifics in table A.2).

Flasks containing 4 mL of medium were shortly flipped upright during irradiation. Therefore some cells were still covered by medium during irradiation and may not have received Bragg peak protons. These cells were removed after irradiation and the remainder was washed and trypsinised. Cells were spun down for 5 minutes at 500xg, resuspended in a small volume of medium and counted. The

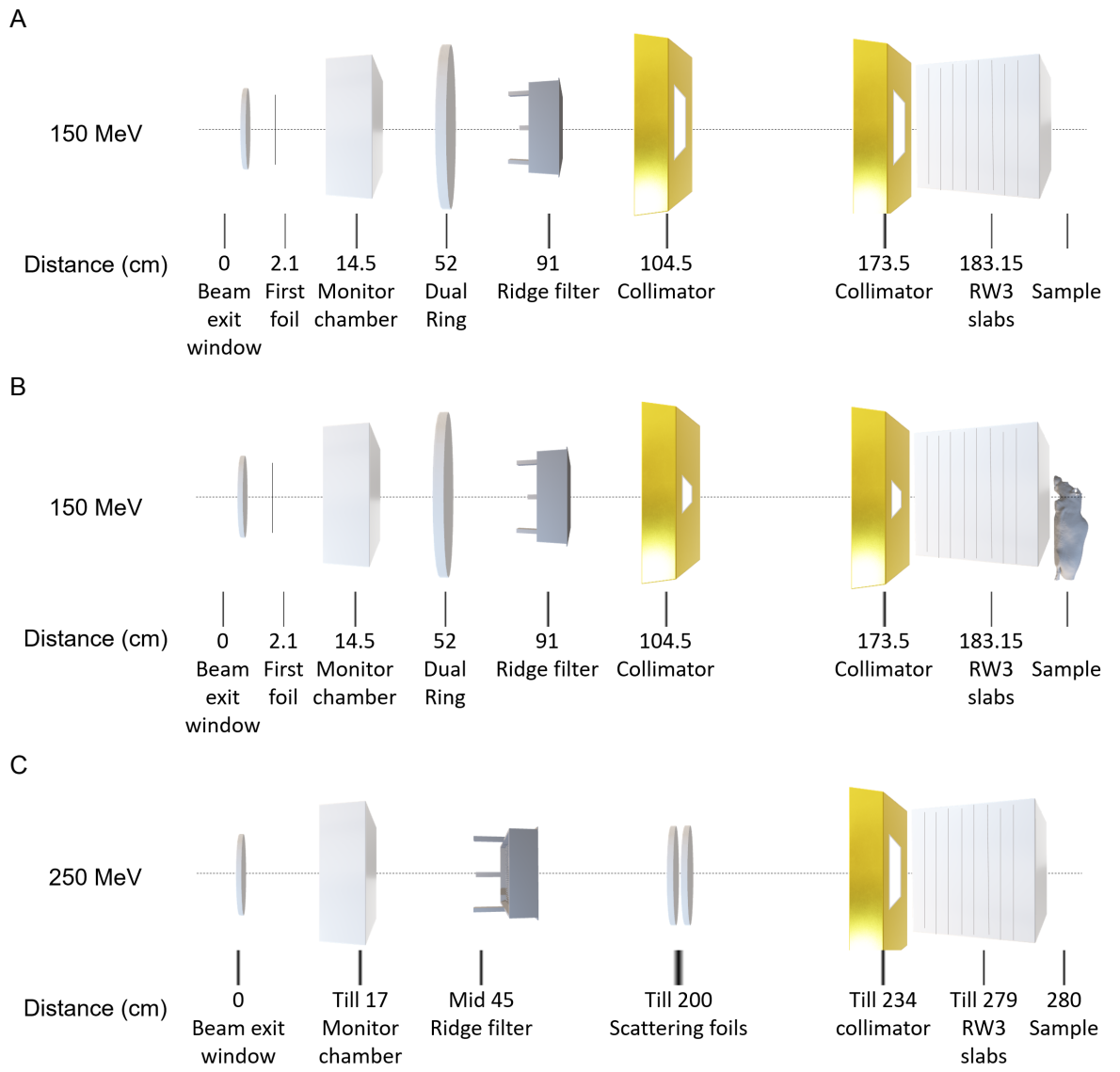

Figure 2.1: **The general beamline component positions for proton irradiations.** The components in the proton beamline and their positions for (A) the conventional in-vitro irradiations, (B) the phantom irradiations, and (C) FLASH irradiations. The components' specifics and differences between experiments are listed in A.2.

FaDu cells were seeded to concentrations of 300, 600, 1200, and 2400 cells/mL for 0, 2, 4, and 6 Gy irradiated samples respectively. Colonies were allowed to form for 14 days, were stained and counted as explained previously for X-ray irradiations.

2.1.3. Inhibitor monotherapy

For U2OS and FaDu, 500 cells were seeded in 6 cm dishes and were allowed to grow overnight. Either, 0, 0.37, 1.1, 3.3, 10 µM of DNA-PKcs inhibitor AZD7648 or 0.11, 0.33, 1.0, 3.0, 9.0 µM of homologous recombination inhibitor B02 was added to the dishes. The cells were incubated with the inhibitors for 7 days at 37°C and 5% CO2 until it was washed away. After 7 and 14 days respectively, U2OS and FaDu were stained and colonies were counted as explained in paragraph 2.1.2.

2.1.4. Irradiation upon DNA damage repair inhibition

FaDu cells were washed, trypsinised, and seeded in 6 cm dishes with 300, 600, 1200, and 2400 cells for 0, 2, 4, and 6 Gy of X-ray respectively. For proton therapy, 360, 720, 1440, and 2880 cells were seeded in T25 flasks for 0, 2, 4, and 6 Gy respectively. Cells were allowed to grow overnight. For

the T25 flasks to be irradiated with protons, cells near the bottom that would be covered by medium when flipped upright were removed. One hour before the irradiation, the cells in both set-ups were supplemented with the required concentration of inhibitor. Cells were irradiated with X-rays or protons in the required doses and colonies were allowed to form. On the seventh day, the medium was refreshed to remove the DDR inhibitor and after 14 days the FaDu cells were stained and colonies were counted as explained in paragraph 2.1.2.

2.1.5. Validation of NHEJ inhibition

Protein isolation

Cells in six cm dishes were washed twice in cold PBS (Lonza Biowhittake BE17-512F), scraped from the dish in 50 µL PBS, and transferred to an Eppendorf tube. They were supplemented with 50 µL 2x Laemmli buffer (4% SDS, 20% glycerol, 120 mM Tris) and boiled for 5 minutes at 95°C to denature the cells. The solution was sheared with a syringe (BD Plastitak 2112057, 25G needle) to reduce the viscosity. At this point, samples can be frozen via liquid nitrogen to perform the Lowry assay later.

Lowry assay

To determine the protein concentration in isolated protein samples a Lowry assay was performed [34]. A calibration curve was prepared using bovine serum albumin (BSA)(0, 2, 5, 10, 15, 20, 30, 40 µg). The protein samples, BSA samples, and Laemmli buffer had a volume of 5 µL and were supplemented with Milli Q water to total volumes of 100 µL. The solutions A (2% Na2CO3 in 0.1 M NaOH) and B (0.5% CuSO4· 5 H2O in 1% sodium citrate, kept dark) were mixed 50:1 directly before use and 1 mL was added to each sample for 10 minutes at room temperature. Folin and Ciocalteus phenoal reagens were diluted 1:2 by water and 100 µL was added to each sample for 30 minutes at room temperature. Of each mixture, 100 µL was put in a 96 well plate and absorbance at 750 nm was measured by Spectromax iD3 (Molecular Devices).

Western blot (Theory in appendix A.1)

25 µg of protein and 1x loading buffer (0.05 Tris, 0.1 M DTT, 2% SDS, 1.5 mM bromophenl blue, 1.1 M glycerol) in 1x Laemmli buffer (2% SDS, 10% glycerol, 60 mM Tris) was heated to 95°C for 5 minutes, cooled shortly, and loaded on a 3-8% Tris-Acetate gradient gel (NuPage EA0378) in 1x Tris-Acetate SDS running buffer (InVitrogen 2399620). The Himark Pre-stained Protein Standard (InVitrogen 2412869, 8.0 µL) was added as protein marker. The gel was run at 50 V until the stacking gel was passed and at 100 V until the gel's end was reached. The holders, sponges and Whatman filter paper were soaked in 2x blot buffer (20% methanol in 1x tris glycine buffer (3 g Tris, 4.5 g glycine in water)) and the Odyssey Immobilin-P transfer membrane (Millipore IPVH00010) was activated for 20 seconds in methanol. The stacking part was removed from the gel before it was added to the assembly. The assembly was put together submerged in 2x blot buffer to avoid air bubbles. The samples were blotted at 300 mA and 4°C for 2 hours while stirring with an icepack.

After blotting, the membranes were cut to size and incubated in blocking buffer (3% skim milk in PBS/Tween-20(0.05%)) for one hour at 4°C at a roller. Next, the membranes were incubated with primary antibody (Rabbit anti-vinculin (1:10000, NB129002, Abcam), Rabbit anti-DNA-PKcs (1:1000, Homemade), Rabbit anti-phospho Ser2056 DNA-PKcs (1:1000, 68716, Cell Signaling Technology)) dissolved in blocking buffer overnight at 4°C on a roller. The blot was washed four times 10 minutes in PBS/Tween-20 (0.05%) at room temperature, after which it was incubated for 1.5 hours on a roller at room temperature with the secondary antibody (1:2000, Anti-rabbit, Jackson ImmunoResearch Labs) dissolved in blocking buffer. The blot was washed again four times 10 minutes in PBS/Tween-20 (0.05%) at room temperature. After adding enhanced chemiluminescence substrate (homemade) to the blots, chemiluminescence was measured with Amersham imager 600 (GE Healthcare) on the automatic mode first, after which incremented measurements were taken with fixed steps of approximately half the automatic exposure time.

2.1.6. Validation of HR inhibition

Transfection of traffic light reporter (TLR)

The following mixtures were prepared using the lipofectamine 3000 kit (Invitrogen L3000-015): solution 1 (125 µL optimem with 5 µL lipofectamine) and solution 2 (125 µL optimem, 1 µL hPiggyBac (120 ng/µL, [35]), 1 µg TLR construct (homemade), 2.5 µL P3000 reagent). The two solutions were mixed

and incubated for 15 minutes at room temperature. The cells were washed with PBS and put in their corresponding medium as described before without penicillin and streptomycin, after which 250 µL of the transfection mixture was added dropwise to the wells of the 6-well plate. The transfection mixture was also added to non-transfected cells in the same medium as a control. After 24 hours, cells were subcultured to a 10 cm dish in culture medium with penicillin and streptomycin. After a day cells were washed with PBS and 1.5 µg/mL puromycin was supplemented to induce selection. Selection continued until non-transfected control cell's survival was negligible.'

Cells were washed, trypsinised, and resuspended to reach single cell populations. Cells were put through a 40 µm cell strainer (Greiner Bio-one), spun down for 5 minutes at 1000 rpm, and resuspended in small volumes of 10% FCS in PBS which had been filtered with a 0.2 µm filter beforehand. Cells were sorted by FACS (Becton, Dickinson and Co.) and non-fluorescent cells were collected in 10% FCS in PBS. These non-flurescent cells do not contain DNA damage in the TLR construct. From this, 85 000 cells were plated in 6 cm dishes.

Flow cytometry-based traffic light reporter assay

U2OS-TLR and FaDu-TLR cells were incubated for 1 hour at 37°C with various concentrations of B02 (Calbiochem 553525, diluted in DMSO). The following mixtures are prepared using the lipofectamine 3000 kit (Invitrogen L3000-015): solution 1 (125 µL optimem with 5 µL lipofectamine) and solution 2 (125 µL optimem, 1 µL hPiggyBac (120 ng/µL, [35]), 1 µg pEX.d14GFP.sEF1a.Kozak.HA.NLS.Sce.T2A.BFP expressing I-Sce I nuclease and GFP donor template (Addgene 45564), 2.5 µL P3000 reagent). The two solutions were mixed and incubated for 15 minutes at room temperature. The cells were washed with PBS and put in standard medium without penicillin and streptomycin, after which 250 µL of the mixture was added dropwise to the wells of the 6-well plate. As a control, non-transfected cells in medium without antibiotics were taken. The cells were grown for two days after which cells were washed in PBS, incubated for 2 minutes at 37°C in trypsin/EDTA, supplemented with 1 mL medium and pipetted up and down to ensure single cell populations. Cells were put through a 40 µm cell strainer (Greiner Bio-one), spun down for 5 minutes at 1000 rpm, and resuspended in 10% FCS in PBS which had been filtered with a 0.2 µm filter beforehand. The samples were analysed by flow cytometry (Becton, Dickinson and Co.) and results were visualised using FlowJo (Becton, Dickinson and Co.).

The flow-cytometry based traffic light reporter assay's theory is explained in appendix A.1.

2.2. Small-animal proton dosimetry

2.2.1. CT calibration

Schneider's CT calibration algorithm

To perform proton dose calculation for treatment planning and to calculate proton ranges from CT scans, the stopping power of each voxel should be determined. To this end, the CT values, measured in Hounsfield Units (HU), should be converted to material properties like mass density and anatomical composition, which together determine the stopping power of tissues. In CT scans, these measured HU values are linked to the mean linear attenuation coefficient along a projection line via

$$H = \left(\frac{\bar{\mu}}{\bar{\mu_{H_2O}}} - 1\right) \cdot 1000 = \left(\frac{\int \hat{f}(E)\mu(E,s)/\int \hat{f}dE}{\int \hat{f}(E)\mu_{H_2O}(E,s)/\int \hat{f}dE} - 1\right) \cdot 1000 \tag{2.1}$$

with E the energy, s the length of the projection line, $\mu(E,s)$ the linear attenuation at a position for a fixed photon energy, and $\hat{f}(E)$ the effective spectrum of a polychromatic X-ray beam (combining source and detector energy spectra). The linear attenuation coefficient µ(E,s) for a fixed energy and position is given as

$$\mu(E) = \rho N_A \Sigma_{i=1}^{n} \left(\frac{w_i}{A_i}\sigma_i(E)\right) \tag{2.2}$$

with ρ the mass density, N_A the Avogadro constant, w_i the elemental weight, A_i the atomic mass, and σ_i the total cross section. From these equations, a conversion between Hounsfield units and the tissue parameters mass density and elemental composition is found. Yet, the energy composition of the polychromatic X-ray beam is unknown, multiple sets of tissue parameters can lead to the same Hounsfield Unit, and many density-elemental composition pairs do not resemble real biological tissues.

To overcome this, Schneider et al. [36] designed an HU to tissue parameter conversion in which tissue parameters are determined for real biological tissues, after which only these parameter sets are converted to HU values instead of mapping all theoretically possible

First, artificial materials with known densities and elemental compositions are scanned. Their HU value is linked to the mean linear attenuation coefficient via formula 2.1 and the mean linear attenuation coefficient itself is determined from tissue parameters via

$$\frac{\bar{\mu}}{\bar{\mu_{H_2O}}} = \frac{\rho \Sigma_{i=1}^{n} \frac{w_i}{A_i}(Z_i + Z_i^{2.86}k_2 + Z_i^{4.62}k_3)}{\rho_{H_2O}\frac{w_H}{A_H}(1 + k_1 + k_2) + \frac{w_O}{H_O}(8 + 8^{2.86}k_1 + 8^{4.62}k_2)} \tag{2.3}$$

with $k_1 = \frac{K^{sca}}{K^{KN}}$, $k_2 = \frac{K^{ph}}{K^{KN}}$. K^{KN}, K^{sca} and K^{ph} describe free electron scattering, coherence and binding energy effects, and photoelectric effect respectively. Together they describe the cross-section of photon-tissue interactions. The coefficients linking the atomic numbers of atoms with their cross sections for the different material-photon interactions were determined by Rutherford et al. [37] The parameters k_1 and k_2 are CT scanner specific and can be determined by performing a least square fit of the difference between calculated HU values (via formula 2.3) and measured HU values.

Next, the HU values are calculated using the fitted cross-section-based coefficients for 71 human biological tissues of which tissue properties were collected by Woodard and White [38, 39]. An HU-density calibration curve is divided into one lung, three soft, and one skeletal tissue region. Tissues are suggested to consist of two types of tissues, e.g. soft tissues consist of water and fat, while skeletal tissues are a mixture of of bone marrow and osseous tissue. The density of an intermediate tissue (e.g. femur tissue) can be calculated from densities of the extremes (red marrow and cortical bone) via

$$\rho = \frac{\rho_1 H_2 - \rho_2 H_1 + (\rho_2 - \rho_1)H}{H_2 - H_1} \tag{2.4}$$

with $H_1 \leq H \leq H_2$. Exemptions to this are the lung region in which densities are computed via simple linear interpolations between air and adipose tissue, and the middle soft tissue region in which all tissues have a common density of 1.03 g/cm3.

The same idea is followed for the elemental compositions of unknown tissues. Here all tissues with HU values in the soft tissue or bone region are given an intermediate of the elemental compositions of the extremes via

$$w_i = \frac{\rho_1(H_2 - H)}{\rho_1 H_2 - \rho_2 H_1 + (\rho_2 - \rho_1)H}(w_{1,i} - w_{2,i}) + w_{2,i}. \tag{2.5}$$

As an exception, all tissues with HU values close to the calculated HU values of air, lungs, and connective tissue are assigned the elemental compositions of these three tissues. Furthermore, the range of soft tissues with densities equal to or exceeding 1.03 g/cm3 are assigned the mean elemental composition of these soft tissues. This is necessary since their differences in elemental compositions cannot be explained by their minor differences in HU values and densities. The acquired HU-density curves and elemental composition regions can be used as input for a Monte Carlo dose calculation software. For each voxel, the measured HU value is converted into material properties and interactions with a simulated proton beam are determined. In a simulation, detectors can be placed from which the proton range in a patient can be measured.

CT imaging

Tissue characterisation phantoms are used for clinical CT scanner calibrations. The phantom is made of water-equivalent material and contains cylindrical inserts with electron densities comparable to human tissues. In this thesis, the Tissue characterisation phantom 467 from Gammex and a phantom fabricated for Erasmus Medical Center by CIRS are used. For the micro-CT scanner calibration, only the inserts are used for practical reasons and for partial elimination of beam hardening effects resulting from larger subjects. The densities and chemical compositions of the inserts are collected in tables 2.1 and 2.2. These artificially created materials mimic biological tissues accurately since their mass densities and effective atomic numbers are close together (see Fig. 2.2).

A tube half-filled with water acts as an initial calibrator. The densities from air and water are 0.0012 and 1.00 g/cm3 respectively, and they consist of 75.5% nitrogen, 23.3% oxygen and 1.3% argon for air and 11.19% hydrogen and 88.81% oxygen for water [36].

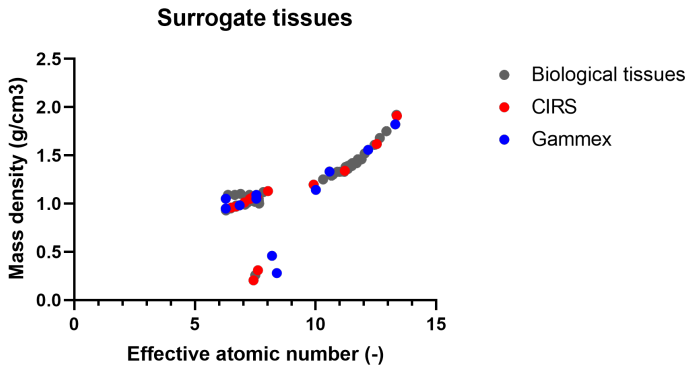

Figure 2.2: **Mass density and effective atomic number of biological tissues and phantom inserts.** The low-density cluster represents lung tissues, the medium density-medium effective atomic number cluster soft tissues, and the high effective number cluster skeletal tissues. Since the CIRS and Gammex inserts describe the biological tissues well, they can be used as substitutes in the CT calibration.

		Density	Elemental composition (%)								
		(g/cm^3)	H	C	N	O	Mg	Si	P	Cl	Ca
455	Lung 300	0.28	7.43	57.86	1.96	20.71	11.19	0.77	0	0.08	0
485	Lung 450	0.46	7.44	58.03	1.97	20.69	11.22	0.57	0	0.08	0
453	AP6 Adipose	0.948	9.44	73.5	2.07	14.86	0	0	0	0.13	0
454	BR-12 Breast	0.983	8.97	71.36	2.14	16.45	0.01	0	0	0.13	0.93
451	CT Solid Water	1.02	Unknown								
481	BRN-SR2 Brain	1.05	9.77	72.13	1.69	16.34	0	0	0	0.07	0
452	Muscle	1.05	8.39	68.5	2.22	18.45	0.03	0	0	0.14	2.26
482	LV1 Liver	1.091	8.4	68.41	2.25	18.5	0.03	0	0	0.14	2.26
456	IB Inner Bone	1.143	6.97	56.73	1.79	19.71	0	0	8.3	0.11	6.38
487	B200 Bone Mineral	1.15	Unknown								
484	CB2 - 30% CaCO3	1.333	5.6	51.77	2.12	28.47	0.18	0	0	0.09	11.77
480	CB2 - 50% CaCO3	1.558	4.03	40.34	1.52	34.13	0.3	0	0	0.07	19.62
450	SB3 Cortical Bone	1.821	2.66	30.34	0.99	39.08	0.41	0	0	0.04	26.48

Table 2.1: **The material properties of Gammex' tissue characterisation phantom model 467 inserts [40].**

		Density	Elemental composition (%)							
		(g/cm^3)	H	C	N	O	Mg	P	Cl	Ca
062a-04	Lung inhale	0.205	8.59	65.92	3.52	19.27	0	0	1.69	1.01
17440014	Lung medium LG3	0.31	7.91	54.78	2.47	25.71	8.14	0	0.95	0
0624-11	Adipose	0.96	9.97	71.36	1.79	16.37	0	0	0.19	0.32
17440009	30% gland + 70% adipose	0.97	9.67	70.72	1.96	16.73	0	0	0.22	0.62
17440010	70% gland + 30% adipose	1.011	9.52	69.8	1.9	17.26	0	0	0.18	1.26
17440011	100% Gland	1.048	9.41	69.13	1.84	17.66	0	0	0.14	1.75
17440001	Soft Tissue Gray	1.055	8.47	57.44	1.65	24.59	7.62	0	0.19	0
17440004	Spinal Cord	1.061	8.46	56.21	1.53	24.78	8.41	0.12	0.18	0.25
17440013	Kidney	1.068	8.52	62.95	1.97	20.63	4.45	0	0.16	1.3
17440005	Brain tissue	1.069	8.16	53.6	1.53	26.49	9.98	0	0.19	0
17440012	Prostate	1.077	7.44	55.8	2.24	25.9	8.41	0	0.2	0
17440003	Spinal disk	1.131	6.71	45.76	1.88	31.06	14.36	0	0.21	0
17440002	Trabecular bone	1.197	7.46	54.84	1.3	25.28	2.12	0	0.11	8.84
17440008	30% cortical + 70% trab.	1.34	6.53	49.85	1.51	23.76	0	5.56	0.07	12.69
17440007	70% cortical + 30% trab.	1.617	4.88	36.92	1.17	29.13	1.21	8.19	0.04	18.44
062MA-19	Cortical bone core	1.91	3.3	25.37	0.91	35.28	3.36	8.82	0.03	22.92

Table 2.2: **The material properties of inserts from CIRS' tissue equivalent CT phantom.** These inserts were created for Erasmus MC and data has been received from the Quality Manager of CIRS [41].

Inserts were scanned in the Quantum Gx2 (PerkinElmer) or VECTor (MILabs) micro-CT scanner on rat waterbeds. Quantum Gx2 scans were performed in the standard mode with a polychromatic X-ray beam with 90 kV as peak voltage, 88 µA acceleration, and a 0.06 mm Cu + 0.5 mm Al filter. The 90 kVp photons could be detected properly since the flat panel's sensitivity has an energy range from 40 to 150 kVp. The image resolution was 72 µm and the field of view for acquisition and reconstruction were 36 mm. The reconstruction method was based on filtered back-projection [21]. Furthermore, 2x2 binning was performed, ring artefacts emerging from deficient detector pixels were removed, and a Ram-Lak filter was applied. This Ram-Lak filter is a high-pass filter in Fourier domain ($H(\omega) = a \cdot \omega$) resulting in pronounced edges and details. The scanner was calibrated after use by scanning a water-filled tube and forcing CT values of air and water to -1000 and 0 HU respectively.

VECTor scans were performed with photons of the maximum energy of 65 kV accelerated by 90 μA. The incorporated filter is 0.5 mm Al. The image resolution was 72 µm and the field of view for acquisition and reconstruction was 36 mm. The scanner was calibrated after use by scanning a water-filled tube and forcing CT values of air and water to -1000 and 0 HU respectively.

The mean HU values and standard deviations were calculated for a circle of 10.8 mm in radius (150 pixels) in the three central slides. Higher-density materials are represented by water-equivalent inserts with an inner core. The HU values from inner cores were measured for circular regions of interest of 6.3 mm in diameter (88 pixels).

CT calibration

The CT scanner-specific k_1 and k_2 parameters were determined by using measured HU values and known tissue properties of CIRS or Gammex inserts with a least square fit of the difference of mean attenuation coefficients determined by HU measurements and by formula 2.3. The determined parameters were used in formula 2.3 to calculate HU values for the artificial inserts and for the listed biological tissues. The mean absolute difference between calculated and measured HU values for soft tissues with lower HU values than adrenal glands and skeletal tissues will be denoted as ΔH_{soft} and ΔH_{bone}.

The HU to density calibration curve was split in 5 sections with the calculated HU values of air, adipose, adrenal gland, small intestine, and yellow/red marrow as starting values. The density for the first section was linearly interpolated between densities of air and adipose, the densities of the third section were fixed to 1.03 g/cm3, and the densities for sections 2, 4, and 5 were calculated with formula 2.4. Here, the input tissues were adipose with adrenal gland, small intestine with connective tissue, and yellow/red marrow with cortical bone.

Known densities and elemental composition of 71 biological tissues were used at input for equation 2.3 with the fitted k-parameters. This results in Hounsfield Units that would be theoretically measured for these biological tissues by the on-site micro-CT scanners. The Hounsfield Unit to chemical composition calibration curve will consist of various regions of Hounsfield units each assigned the elemental composition of one or a combination of the 71 biological tissues. consists of various step functions. For example, tissues with $-1000 \leq HU < -950$ and $-950 \leq HU < CT_{adipose}$ were given the elemental composition of air and lungs respectively. The region between calculated CT values of adipose and adrenal gland was split in multiple sections of $2 \cdot \Delta H_{soft}$. The average HU value of a section and the properties of adipose and adrenal gland were used in formula 2.5 to determine chemical compositions of these sections. The composition of connective tissue was given to all HU values of $[H_{connective\ tissue} - \Delta H_{soft}, H_{connective\ tissue} + \Delta H_{soft}]$. The complete HU region between the previous mentioned soft tissues and connective tissue was given the mean composition of all biological tissues within this HU region. At last, the region above $H_{connective\ tissue} + \Delta H_{soft}$ was assigned as skeletal tissue. This region was split in multiple sections of $2 \cdot \Delta H_{bone}$ and the average HU value of a section and the properties of yellow/red marrow and cortical bone were used in formula 2.5 to determine chemical compositions of the skeletal tissue sections.

2.2.2. Phantom design and printing

Murinemorphic mouse phantom design goals

Based on micro-CT images of a mouse and the HU to material properties conversion, an estimate for the proton range can be made. During in vivo experiments, the dose distribution around the tumour cannot be measured, since this requires the addition of dosimeters invasively. Therefore, a murinemorphic phantom was designed in which the dose distribution can be measured. Murinemorphic phantoms

are 1:1 models of real mice which are optimised on geometry and composition and are often used to check new developments in clinical practice. This new term is an alternative to anthropomorphic, which means 'resembling human'.

Three design requirements were defined upfront which if achieved lead to a mouse phantom suitable for dose distribution estimations of real mouse proton irradiations. First, the phantom should resemble a real mouse, meaning that its geometry should match mice's and its materials should match mouse tissues regarding mass density. To reach this, the phantom's geometry was based on real mice CT scans and was 3D printed accordingly. The materials used were chosen based on their densities.

Secondly, it should be possible to measure the dose distribution around the tumour resulting from irradiation. Therefore, the phantom's head was split in several segments in between which EBT3 gafchromic films were placed. Upon irradiation, polymerisation within the film takes place, leading to the blue colouring of the film [42]. From the film's optical density, the radiation dose can be determined.

At last, the phantom's tumour should be visible on CT scans to allow for treatment planning. The tumour should thus be made from a material with a significantly different electron density than the other materials.

Anatomical segmentation

The phantom's geometry was based on a full-body mouse micro-CT scan by the Quantum Gx2 scanner received from the AMIE facility. Within MATLAB [43], the anterior and posterior scan were combined, the image was cropped and rotated, and the mouse bed was removed from the image. The image was segmented and labelled via Otsu thresholding with two thresholds for the air-soft tissue and soft tissue-bone boundaries. Fully enclosed small labelled regions were incorporated in the surrounding larger labelled region.

The second largest air-region was labelled as lungs. A closing operation was performed to fill the holes. The total lung region was split in superpixels and centroids were determined. Based on this, superpixels located in the trachea were labelled air instead of lungs.

A spherical tumour of 5.34 mm in diameter was placed in the phantom's head and neck region in between the left and right mandible (jawbones) directly ventral from the air-filled pharynx. It was placed without intersecting bones nor leaving the body. The complete phantom was split into five pieces: the main bulk and four 2.67 mm thick segments to be inserted in the head in dorsal-ventral orientation. The segments span the dimensions from 2.67 mm ventral until 8.01 mm dorsal of the tumour's center, meaning that the two ventral segments contain exactly half of the tumour. Dorsal of the segments, 0.688 mm was labelled as air, to make space for EBT3 films to be inserted.

The labelled five pieces were saved in DICOM format and converted into 3D-printer compatible .stl files via Slicer [44, 45].

Phantom materials

The lungs, soft tissues, and bones have mass densities of 0.26, 0.93-1.12, and 1.1-1.92 g/cm3 respectively [39]. Tumours in general have mass densities close to but slightly higher than surrounding soft tissues. Therefore, the soft tissues, tumour, and bones were printed with HIPS (1.08 g/cm3), transparent HIPS (1.08 g/cm3), and PLA (1.17 g/cm3) respectively.

For the bones, a plastic with a rather low density was preferred over higher density materials consisting of metals, since the latter varies too much from biological tissues regarding its elemental composition.

A low-density material for the lungs was not available, so PLA was printed with an infill percentage of 26% to reach a density of 0.30 g/cm^3 accurately mimicking the low-density lungs.

3D Printing

The phantom was printed in five pieces with the Ultimaker 3 (Ultimaker) printer by DEMO Delft. The bulk was printed from the dorsal to ventral side with layers of 0.1 mm. The four segments from the head were printed flat with layers of 0.1 mm. The soft tissue and bones were printed together by filling the two nozzles with HIPS and PLA respectively. The area of the lungs was filled with PLA using a infill of 26%, to have a low-density region. A separately printed HIPS sphere of 2.5 mm in radius was inserted in between the head segments afterwards.

CT contrast check
An assembly of three quarter of a PLA cylinder of 60 mm in height and 30 mm in diameter containing a double HIPS cone was printed with the Ultimaker 3 (Ultimaker) by DEMO Delft with layers of 0.1 mm. Both the assembly and the phantom were imaged with the QuantumGx2 micro-CT scanner (PerkinElmer) with the same settings as explained in 2.2.1.

2.2.3. Phantom irradiation

Film output to dose calibration
Nine gafchromic EBT3 films (Ashland Speciality Ingredients) were split in two of which one part was kept as non-irradiated background control and the other was irradiated with 0.5, 1, 2, 3, 4, 5, 6, 8, or 10 Gy. Films were scanned with a frame in the Expression 12000 XL scanner (Epson) with Epson Scan 2 software as 48-bit colours at 75 dpi resolution. The scans were corrected for lateral scan effects [46] by an in-house python script of Holland PTC.

In ImageJ [47] the red channel was analysed since this channel contains most contrast upon irradiation. Its gray values were converted into optical densities via $OD = log_{10}\,(2^{16} \,/\, grayvalue)$. The background value was determined from a ROI of 320x80 pixels (10.8x2.7 cm) of the non-irradiated EBT3 film piece and subtracted from the irradiated film optical density values. From the dose distribution, the center of mass was determined and from the central ROI of 160x160 pixels (5.4x5.4 cm) the mean and standard deviation optical density was measured. A horizontal line through the center of mass was used to measure the optical density profile. The mean optical densities were fitted for $OD(D) = a + b/(D - c)$.

Phantom irradiation and dose profiles
The murinemorphic phantom with six inserted EBT3 films was irradiated with 5 Gy. It was positioned such that the end of the SOBP matched the distal edge of the artificial tumour. For this, the determined range from the CT calibration based on a real mouse and the WET of 0.11 mm of the EBT3 films were taken into account, leading to the necessity of 12.3 cm of RW3 slabs to stop the protons just behind the tumour. The complete beamline consisted of a foil scatterer at 3.5 cm, the beam monitor at 20 cm, a thin dual ring at 45 cm, a 2x2 cm collimator, a ridge filter, a second 1x1 cm collimator, and 12.3 cm of RW3 slabs placed just in front of the phantom at 200 cm. A schematic representation is shown in figure 2.1 and further specifics in A.2.

After irradiation, the inserted gafchromic EBT3 films were scanned within a frame by the EPSON Expression 12000XL to 75 dpi 48-bit colour scans. The scans were corrected for lateral scan effects by an in-house python script of Holland PTC. The red channel was chosen and converted into optical density. The mean optical density from the non-irradiated films from the previous experiment was removed from the optical density values and the dose was determined from the fitted optical density to dose formula.

2.2.4. Monte Carlo simulation

Physics settings
In TOPAS, the default modules with physics settings were used. These are *g4em-standard_ opt4, g4hphy_ QGSP_ BIC_ HP, g4decay, g4ion-binarycascade, g4h-elastic_ HP, g4stopping* describing electromagnetic interactions, nuclear interactions via the binary cascade models, decay of excited residual nuclei, nuclear interactions of light ions via the binary cascade model, elastic scattering, and capture of charged particles at rest respectively [48].

Source settings proton beam
The source created a proton beam of 30 million protons with and initial mean energy of 150 MeV and 0.25% spread. The settings of the proton beam were determines in previous research within Holland PTC [48]. The elliptical beam followed a Gaussian distribution with cut-offs at 10 cm and lateral spreads in x an y of 0.24 and 0.18 cm respectively. The angular cut-off was placed at 90 degrees with a spread of 0.0032 and 0.0034 rad in x and y respectively.

Geometry beam line
A lead foil of 3 mm in thickness was placed at 2.1 cm from the exit window. Next, the beam monitor was placed at 14.5 cm from the exit window. Although the beam monitor is 6.7 cm thick, the BM1

was simulated as water with a water-equivalent thickness of 0.022 cm. The protons will further travel through the dual ring at 52 cm from the exit window where they are scattered. The dual ring contains an inner lead circle of 5.5 mm in radius and 1.5 mm thick and an outer aluminum ring around of 100 mm in radius and 5.0 mm thick. The ridge filter at 91 cm from the exit window was imported from stl files received from the manufacturer via Angeline Meijer [49]. Furthermore, two brass collimators of 7 cm thickness and 32 by 32 cm in size were positioned at 104.5 and 173.5 cm from the exit window. The first contained a hole of 2 by 2 cm and the latter of 1 by 1 cm. The water-equivalent RW3 slabs were placed touching the second scatterer. The center of the 12.3 cm of RW3 was thus positioned at 183.15 cm. At last, with a small section of air between the RW3 slabs and the mouse, the materials originating from micro-CT scans were placed at 192.3 cm.

Imaging to material conversion
The micro-CT scan was converted to materials by the build-in converter based on Schneider's algorithm [36, 50]. Here for each voxel, a density and elemental composition is determined. As input, the CT calibration using QuantumGX2 scans of CIRS inserts were used (Table 2.3).

TOPAS property	Input	Explanation
	Density	
dv:Ge/Patient/Density-Correction	4096 *4096 ones*	Default setting
iv:Ge/Patient/Schneider-HounsfieldUnitSections	6 -1024 -186 -30 2 52 3071	HU region boundaries of the density curve
uv:Ge/Patient/Schneider-DensityOffset	5 1.14388 1.04949 1.03 1.02743 1.03955	Parameter b in calibration curve $\rho = a \cdot HU + b$
uv:Ge/Patient/Schneider-DensityFactor	5 0.00114396 0.000639078 0 0.0018005 0.000391712	Parameter a in calibration curve $\rho = a \cdot HU + b$
uv:Ge/Patient/Schneider-DensityFactorOffset	5 0 0 0 0 0	Not necessary for density formula
	Elemental composition	
iv:Ge/Patient/Schneider-HUToMaterialSections	32 -1024 -950 -186 -170 -150 -130 -110 -90 -70 -50 -31 40 60 220 380 540 700 860 1020 1180 1340 1500 1660 1820 1980 2140 2300 2460 2620 2780 2940 3071	HU boundaries of elemental composition sections
sv:Ge/Patient/Schneider-Elements	9 Hydrogen Carbon Nitrogen Oxygen Magnesium Phosphorus Chlorine Argon Calcium	Atom types in elemental composition
uv:Ge/Patient/Schneider-MaterialsWeight1	9 0 0 0.755 0.232 0 0 0 0.013 0	Fraction of atoms in air (sum to 1)
uv:Ge/Patient/Schneider-MaterialsWeight2	9 0.106581 0.307067 0.024606 0.560804 0 0.000942 0 0 0	Fraction of atoms in lung (sum to 1)
Continue until 31	...	...
	Visualisation	
iv:Gr/Color/PatientTissue1	3 63 63 63	RGB colour for air voxels in visualiser
iv:Gr/Color/PatientTissue2	3 100 22400 0	RGB colour for lung voxels in visualiser
Continue until 31	...	...

Table 2.3: **TOPAS parameters for imaging to material conversion.** The inserted values originate from the CT calibration with QuantumGx2 scanned CIRS inserts.

Scoring elements
Several scorers were created in the virtual world, due to which they can measure physical properties without interacting with the particles. In this simulation, a 2 cm thick dose-to-medium scorer was placed orthogonal to the proton beam at the isocenter at 91 cm. This scorer was 30 by 30 cm in size discretised into 150 by 150 bins. Furthermore, in the mouse dose-to-medium scorers were positions at approximately 191.5, 191.8, 192.1, 192.4, 192.77, and 193.3 cm. The 1 mm thick detectors were 2 by

4 centimeters in size discretised into 50 by 50 bins. At last, a scorer was placed from x=-7.5 to x=7.5 cm from a depth of 161.8 till 201.8 cm. This horizontally placed scorer was 2 cm thick and contained 75 bins in x and 200 bins in z.

2.3. Proton FLASH irradiations

2.3.1. Cell culture

The head and neck squamous cell carcinoma-derived cell line FaDu was cultured in an equal volume mixture of Dulbecco's modified Eagle's medium (Gibco 41966-029) and Ham's F10 (Biowest L0140) with 10% fetal bovine serum and 1% penicillin-streptomycin (Sigma-Aldrich P0781). They were split twice a week by washing them with Phosphate Buffered Saline (PBS, Lonza Biowhittake BE17-512F), incubating them 5 minutes in a trypsin/EDTA (Sigma-Aldrich T3924) solution to detach, and transferring a sixth to the next plate. The cells were incubated at 37°C and 5% CO2.

2.3.2. Cell irradiations

Cells were seeded in wells of 24-well plates (Biofil) with 167 000 cells in 1 mL the day before the irradiation to adhere and form a monolayer. Before irradiating, the wells were completely filled with medium and sealed with plate seals (InVitrogen).

Before irradiating, dosimetry was performed by two irradiations with 250 MeV protons for 10 seconds and counts were measured by the Markus chamber (PTW). Together with the measured atmospheric pressure and temperature, the dose rate could be determined.

The complete beamline consisted of the beam monitor at 17 cm of the exit window, a ridge filter at 45 cm, two scattering foils at 200 cm, a 10x10 cm collimator at 234 cm, and 10.3 or 29.0 cm of RW3 slabs placed just in front of the 24 well plates in a vertical stage at 280 cm. The position of this vertical stage made by DEMO (Delft) could be controlled in the control room. A schematic representation is shown in figure 2.1 and further specifics in A.2.

Cells were irradiated with 250 MeV protons at 800 nA with doses of 2, 4, 6, or 8 Gy. After the irradiation, cells were washed and trypsinised. Cells were counted in small volumes and were seeded in 6 cm dishes with 300, 600, 1200, and 2400 cells per dish for 0, 2, 4 and 6 Gy respectively. Cells were allowed to form colonies, were stained, and counted as explained in paragraph 2.1.2.

3

Results

3.1. Radiosensitisation by DNA damage repair inhibition

Since both x-ray and proton irradiation induce apoptosis by damaging the DNA, inhibition of DNA damage repair may exaggerate this effect. In this thesis, inhibitors for non-homologous end-joining and homologous recombination were used in combination treatments with x-ray and proton irradiations to check for potential radiosensitising effects.

3.1.1. Radiosensitisation by non-homologous end-joining inhibition

The small-molecule inhibitor AZD7648 was investigated to assess whether it could increase radiosensitivity for x-ray or proton irradiation. This molecule inhibits the autophosphorylation of DNA-PKcs [17]. When non-phosphorylated DNA-PKcs is recruited towards a double-stranded break by the Ku70/Ku80 dimer, repair cannot start yet. Only upon autophosphorylation of DNA-PKcs, the two DNA ends are exposed and repair machinery can bind to it and ligate the ends [12].

To determine the optimal concentration of AZD7648 to inhibit phosphorylation of DNA-PKcs without inducing toxicity for the cells via other pathways, the toxicity and DNA-PKcs phosphorylation rates were determined for several concentrations of AZD7648.

Both U2OS and FaDu were supplemented with AZD7648 in concentration ranging from 0 to 2.5 µM for 7 days. This monotherapy led to the overall survival as shown in figure 3.1a. The small-inhibitor molecule was not toxic for U2OS cells, while FaDu cells are compromised in survival upon incubation with AZD7648. The survival rates dropped from 100% to 80% for concentration above 0.09 µM, and even to 50% from 0.83 µM AZD7648.

To assess the inhibition of DNA-PKcs autophosphorylation by AZD7648, the amount of phospho-DNA-PKcs (pSer2056) was determined using westernblot. Total DNA-PKcs was also measured to make sure that the total amount of protein was not altered due to the inhibitor treatment. All samples were irradiated with 8 Gy X-ray to induce sufficient DNA-PKcs phosphorylation and a range of 0-10 µM AZD7648 was tested. Upon irradiation the expression of phosphorylated DNA-PKcs increases strongly (Fig. 3.1b, full western blots in appendix A.3). With an increasing concentration of the small-molecule inhibitor AZD7648, the expression of Ser2056 phospho-DNA-PKcs decreases, while it does not influence the total amount of DNA-PKcs.

The western blot signals were quantified and phospho-DNA-PKcs and DNA-PKcs signals were normalised to the loading control vinculin. The expression of phospho-DNA-PKcs is almost absent without DNA damage induction. Upon X-ray irradiation, it increases strongly, and drops with increasing AZD7648 concentration (Fig. 3.1c). This effect is more pronounced for FaDu then U2OS cells. Division of phospho-DNA-PKcs expression levels by DNA-PKcs expression levels and normalisation of phospho-DNA-PKcs expression by the expression level at 0 µM AZD7648 allows for easier comparison between U2OS and FaDu cells (Fig. 3.1d). A major expression drop towards 37% is reached for U2OS cells with 1.0 µM AZD7648, while DNA-PKcs phosphorylation in FaDu cells drops to 37% by

addition of 0.11 µM AZD7648 already.

It was concluded to use concentrations for FaDu cells between 0.1 µM and 1.0 µM of AZD7648 to include conditions with minor toxicity and almost 3-fold DNA-PKcs phosphorylation inhibition and conditions with stronger 10-fold inhibition at the cost of higher toxicity.

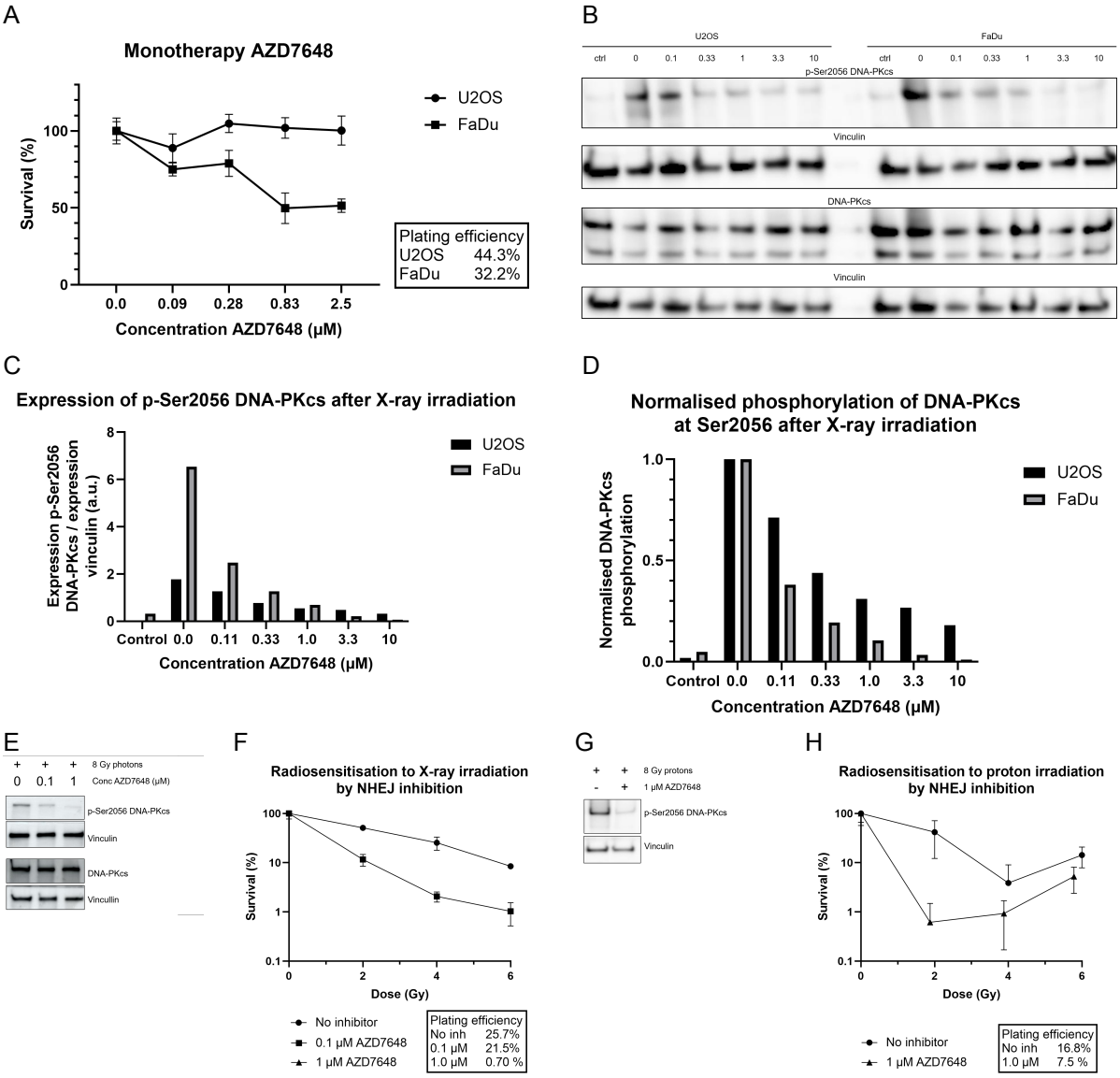

Figure 3.1: **Radiosensitisation of X-ray/proton irradiation by non-homologous end-joining inhibition.** (A) The toxicity of the small-molecule inhibitor AZD7648 and (B) its effect on expression levels of phospho-DNA-PKcs and total DNA-PKcs. (C) Phospho-DNA-PKcs expression levels normalised by vinculin loading controls. (D) Relative phospho-DNA-PKcs expression compared to total DNA-PKcs expression normalised to the 0 µM condition. Combination therapies of x-ray and proton irradiation with properly functioning AZD7648 (E,G) showed clear sensitivity enhancement to X-ray by AZD7648 (F), but no clear trend for proton irradiations (H).

Since the, from head and neck squamous cell carcinoma originating, FaDu cells are the cell line of interest, they were used for combination therapies of radiation and AZD7648. Cells were irradiated with 0-6 Gy of x-rays combined with 0, 0.1 or 1.0 µM AZD7648 for 7 days. Three separate control samples were irradiated with 8 Gy x-rays to validate whether DNA-PKcs phosphorylation was inhibited by the small-molecule inhibitor. The phosphorylation inhibition by AZD7648 was successful for both 0.1 and 1.0 µM with a larger decrease in expression after incubation with 1.0 µM AZD7648 (Fig. 3.1e, full western blots in appendix A.3). Cells receiving 1.0 µM AZD7648 experienced poor survival with survival rates below 0.7% (Fig.3.1f). Since even the unirradiated cells incubated with 1.0 µM AZD7648

showed poor survival, this condition could not be analysed further. The cells incubated with 0 and 0.1 µM AZD7648, however, had proper plating efficiencies of >20%. Clonogenic survival drops to 8.50 and 1.03 % for cells receiving 6 Gy x-ray with 0 and 0.1 µM AZD7648 respectively. Both survival curves do not fit the linear-quadratic model, so α and β parameters cannot be compared. Yet a clear significant radiosensitisation effect of 0.1 µM AZD7648 for x-ray radiation is detected as standard deviations do not overlap.

This experiment was repeated with proton therapy, so cells were irradiated with 0-6 Gy of protons upon incubation with 0 or 1.0 µM AZD7648. Furthermore, two control samples were irradiated with 8 Gy and incubated with or without inhibitor to validate whether DNA-PKcs phosphorylation was blocked by AZD7648. The expression of phospho-DNA-PKcs indeed showed major decrease upon irradiation with 1.0 µM AZD7648 (Fig. 3.1g, full western blot in appendix A.3). The plating efficiencies were 25.7 and 16.7% for non-irradiated cells without and with AZD7648 respectively, so 1.0 µM of AZD7648 already induced some toxicity (Fig. 3.1h). Both curves show a drop in survival followed by an increase in survival. This does not meet any expectations of survival curves, and thus conclusions cannot be drawn from these results.

The small-molecule inhibitor successfully blocks phosphorylation on Serine 2056 of DNA-PKcs, with a larger effect on FaDu cells than U2OS cells. It is not toxic for U2OS cells, while FaDu cells experience minor toxicity from 0.1 µM and major toxicity from 0.8 µM AZD7648. No conclusions can be drawn about radiosensitisation of AZD7648 on proton irradiations of FaDu cells from this experiment, while a clear radiosensitising effect was observed in FaDu for X-ray irradiation.

3.1.2. Radiosensitisation by homologous recombination inhibition

Besides the non-homologous end-joining inhibitor AZD7648, an inhibitor for homologous recombination was investigated. B02 was found to inhibit the binding of RAD51 to the DNA [18]. Usually binding of RAD51 to the single stranded DNA near a double-stranded break, induces the formation of a filament which searches for DNA homologous to the ssDNA overhang. The latter acts as a template for DNA synthesis. Inhibition of RAD51 binding to the DNA thus leads to the incapability to find homologous DNA and repair the double-stranded break.

To determine the optimal concentration of B02 during combination therapies with radiation, its toxicity to cells without radiation and efficiency to block homologous recombination had to be assessed.

Both U2OS and FaDu cells were incubated for 7 days with 0.0 until 9.0 µM of B02. The clonogenic survival was not compromised by B02 for U2OS, but for FaDu cells survival was compromised for concentrations exceeding 1.0 µM (Fig. 3.2a).

The efficiency of homologous recombination inhibition was determined via a flow cytometry-based traffic light reporter assay in which the execution of homologous recombination results in green fluorescence and non-homologous end-joining may lead to red fluorescence (see appendix A.1). This yielded multiple graphs per condition showing the GFP and mCherry signal at the vertical axis (Fig. 3.2b). Whenever GFP and mCherry signals exceeded the gate determined from the uncut cells, they were indicated as positive for either GFP or mCherry. In general GFP and mCherry signals are proportional to homologous recombination rates and non-homologous end-joining rates respectively. Analysis of the percentage of cells positive for GFP and mCherry, did not yield any trends with the concentration of B02 (Fig. 3.2c,d). Therefore, the efficiency of B02 to inhibit homologous recombination has not been observed.

Since no major toxicities were observed in U2OS and FaDu cells for concentrations until 1.0 µM, and no clear effect of B02 on homologous recombination nor non-homologous end-joining had been observed, the maximum non-toxic concentration of B02 was used in combination therapies.

Combination treatments of X-ray irradiation with or without 1.0 µM B02, showed highly similar clonogenic survival for the FaDu cell line (Fig. 3.2e). For combination treatments with proton therapy, no clear comparison can be made since especially the cells incubated with B02 during irradiation show decreasing survival followed by increasing survival with increasing dose (Fig. 3.2f).

To conclude, the small-molecule inhibitor B02 is not toxic for U2OS, but is toxic for FaDu cells for concentrations exceeding 1.0 µM. Its efficiency to inhibit homologous recombination could not be shown,

since no trends appear for GFP and mCherry positive cells upon irradiation in combination with increasing B02 concentrations. The molecule does not have any effect on clonogenic survival after x-ray irradiation, but conclusions on its effect on proton irradiations cannot be made.

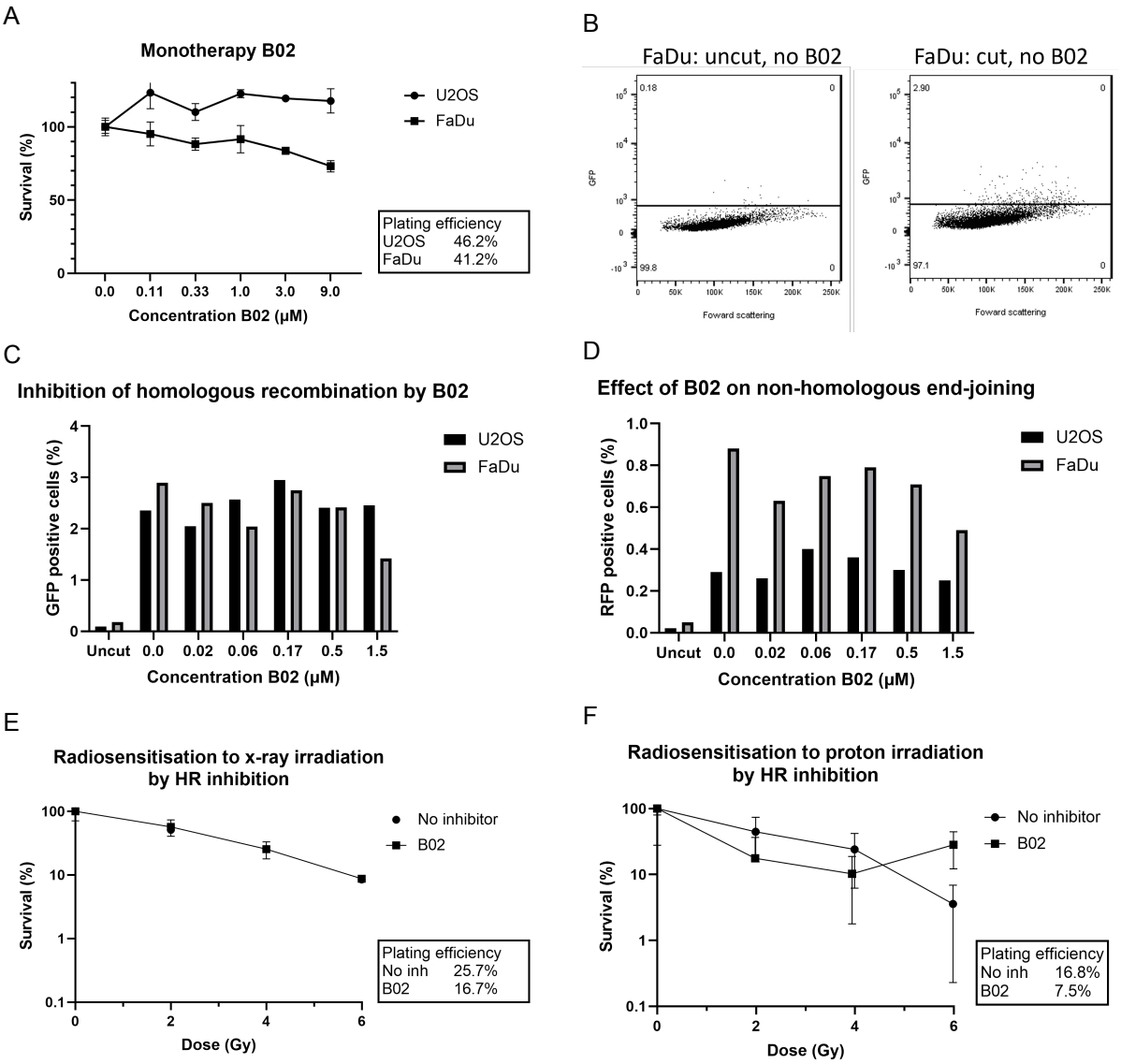

Figure 3.2: **Radiosensitisation of X-ray/proton irradiation by homologous recombination inhibition.** (A) The toxicity of the small-molecule inhibitor B02. (B) An example of flow-cytometry results with dots above the gate indicating cells positive for GFP and mCherry respectively. Increasing concentrations of B02 do not affect the percentage of GFP positive cells (C) nor mCherry positive cells (D) in a clear manner. (E) The addition of B02 to x-ray irradiated FaDu cells does not have any effect on clonogenic survival, while (F) no trend nor clear effect can be observed for proton irradiated FaDu cells upon B02 incubation.

3.2. Small-animal proton dosimetry

The performance of small animal Bragg peak irradiation depends on accurate range determination of proton within the mouse. Therefore, a micro-CT scan exposing the animal's anatomy is executed and CT values are converted into material properties via the stoichiometric method of Schneider et al. [36] Validation of material properties assignment and relative stopping power estimation of biological tissues will first be performed by comparison with calculated and measured stopping power ratios. At last, proton irradiation of a 3D printed murinemorphic phantom allows for validation of the in vivo proton range.

3.2.1. Micro-CT calibration

The conversion of measured Hounsfield Units to relative stopping powers is performed via Schneider's method [51] in which CT scanner specific parameters are derived from scans of phantom inserts with known material properties. From this, CT values are determined for 71 real biological tissues, and interpolations of these tissues yield CT to material properties mappings for all HU values.

CIRS and Gammex inserts were scanned by the QuantumGx2 and VECTor micro-CT scanners. The measured Hounsfield units of inserts scanned by the VECTor system exceeded measured Hounsfield Units of the same insert by the QuantumGx2 scanner 3.1. The mean HU values for a circular region of interest in the center of the insert of air and water did not equal -1000 and 0. The calibration to air and the mousebed of water-equivalent material during CT scanning thus had not succeeded and HU values were forced to -1000 and 0 HU. A linear interpolation was used to alter the measurements of other inserts with respect to air and water. Besides the differences in mean HU values between the scanners, standard deviations of measured HU values are larger in VECTor scans than QuantumGx2 scans.

CIRS phantom			Gammex phantom		
Insert	CT value +- SD (HU)		Insert	CT value +- SD (HU)	
	QuantumGx2	VECTor		QuantumGx2	VECTor
Air	-1040.3 +- 17.5	-1016.1 +- 118.8	Air	-998.1 +- 23.1	-1000.2 +- 90.0
Lung inhale	-843.3 +- 40.2	-832.7 +- 103.1	Lung 300	-804.1 +- 237.8	-702.9 +- 304.9
Lung medium	-760.7 +- 23.8	-734.1 +- 117.8	Lung450	-657.4 +- 187.1	-534.3 +- 276.3
Adipose	-270.7 +- 27.2	-237.7 +-183.7	Adipose	-288.9 +- 62.5	-280.4 +- 156.7
30% gland + 70% adipose	-238.1 +- 27.7	-190.3 +- 189.7	Breast	-197.8 +- 66.2	-146.4 +- 173.9
Water	-112.4 +- 26.7	-12.2 +- 174.5	Water	65.7 +- 70.0	20.0 +- 121.3
70% gland + 30% adipose	-193.4 +- 35.8	-81.3 +- 208.7	Brain	-178.4 +- 60.4	-166.8 +- 166.1
100% Gland	-127.0 +- 28.7	-4.8 +- 220.2	Muscle	-52.9 +- 74.5	47.4 +- 204.7
Soft Tissue	-135.2 +- 29.8	-21.7 +- 221.2	Liver	-17.4 +- 75.3	86.4 +- 207.7
Spinal Cord	-119.7 +- 30.2	22.9 +- 226.3			
Kidney	-93.9 +- 34.4	55.4 +- 234.0			
Brain	-105.0 +- 31.9	55.7 +- 233.5			
Prostate	-120.3 +- 30.2	18.3 +- 227.6			
Spinal disk	-22.2 +- 33.0	183.9 +- 252.1			
Trabecular bone	293.3 +- 57.4	880.5 +- 399.4	Inner bone	382.3 +- 96.6	728.8 +- 314.4
30% cortical + 70% trabecular	621.1 +- 67.3	1547.8 +- 550.9	CB2 30% CaCO3	706.1 +- 95.0	1208.0 +- 394.6
70% cortical + 30% trabecular	1120.7 +- 80.0	2717.1 +- 891.8	CB2 50% CaCO3	1301.1 +- 129.0	2161.7 +- 604.8
Cortical bone core	2039.4 +- 39.4	3916.8 +- 513.7	Cortical bone	1875.5 +- 163.6	3191.7 +- 900.1

Table 3.1: **Raw data of micro-CT scans of surrogate phantom inserts.** The mean and standard deviation of CT values in a region of interest of the three central slices per CIRS or Gammex insert.

This is confirmed by visual investigation of adipose inserts (Fig. 3.3a). All QuantumGx2 scans had

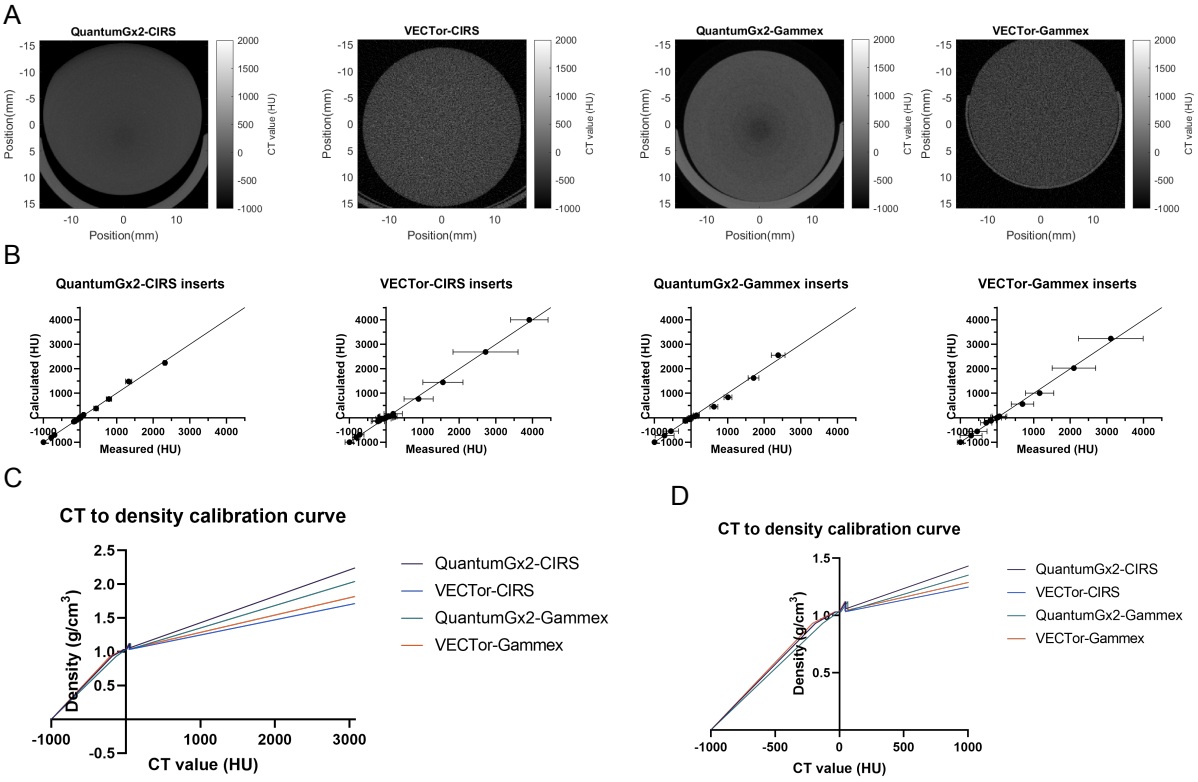

Figure 3.3: **Micro-CT calibration from Hounsfield Units to density.** (A) Micro-CT scans of adipose resembling inserts of CIRS and Gammex phantoms. (B) Comparison of measured CT values with calculated CT values using the fitted CT-scanner specific k-parameters. (C) The relation between measured CT values and density as determined by the four calibration set-ups. (D) A zoomed view of the CT to density calibration curve showing soft tissues (approximately $-150 < CT < 50$) are mapped by multiple segments.

homogeneous CT values for single inserts while VECTor scans contained more noise. Besides this, QuantumGx2 scans had dark spots with surrounding rings in the image's center, which was either mildly or strongly visible in all scans.

Least-square minimisation of the difference between attenuation coefficients of inserts determined via real material properties or measured HU values, yields two scanner-specific parameters 3.2. No major dependence of k-parameters on either scanner nor phantom an be observed. With the fitted k-parameters, HU values are calculated for the inserts and compared with the measured values 3.3b. Since VECTor scans of inserts yield higher CT values than QuantumGx2 scans, the calculated CT values are higher as well. Furthermore note that the errorsbars in the measured CT values by the VECTor scans originate from the noise in these images.

	Schneider et al [36]	QuantumGX2 -CIRS	VECTor -CIRS	QuantumGx2 -Gammex	VECTor -Gammex
k_1	1.24 E-03	1.35 E-02	2.90 E-03	2.13 E-02	1.10 E-02
k_2	3.06 E-05	4.04 E-05	1.90 E-04	4.37 E-10	1.47 E-04

Table 3.2: **Fitted k-parameters during CT calibration.** k_1 compares coherence and binding energy effects with free electron scattering, and k_2 compares photoelectric effect rates with free electron scattering rates.

From the measured CT values for inserts, the fitted k-parameters, and the material properties of 71 biological tissues, a mapping from CT value to density and elemental composition can be created via the method of Schneider et al. [36] The CT value to density mapping contains five continuous regions for low-density tissues, soft tissues (3x), and skeletal tissues (Fig. 3.3c). From the four methods highly similar curves are determined for the low-density and soft tissue regions, yet deviations appear for the skeletal tissues. In general, results from methods with the same micro-CT scanner used are closer together than from the same phantom inserts. The micro-CT scanner thus highly affects the results.

Tissue	CT range (HU)		Elemental composition (%) H	C	N	O	Mg	P	Cl	Ar	Ca
Air	-1024	-950	0.00	0.00	75.50	23.20	0.00	0.00	0.00	1.30	0.00
Lung	-950	-186	10.30	10.50	3.10	75.90	0.00	0.20	0.00	0.00	0.00
Soft tissue	-186	-170	11.54	65.60	0.35	22.51	0.00	0.01	0.00	0.00	0.00
Soft tissue	-170	-150	11.41	60.66	0.65	27.26	0.00	0.02	0.00	0.00	0.00
Soft tissue	-150	-130	11.28	55.31	0.97	32.40	0.00	0.03	0.00	0.00	0.00
Soft tissue	-130	-110	11.15	50.11	1.29	37.41	0.00	0.05	0.00	0.00	0.00
Soft tissue	-110	-90	11.02	45.04	1.59	42.29	0.00	0.06	0.00	0.00	0.00
Soft tissue	-90	-70	10.89	40.10	1.89	47.04	0.00	0.07	0.00	0.00	0.00
Soft tissue	-70	-50	10.77	35.29	2.18	51.67	0.00	0.08	0.00	0.00	0.00
Soft tissue	-50	-31	10.66	30.71	2.46	56.08	0.00	0.09	0.00	0.00	0.00
Mix soft tissues	-31	40	10.34	13.08	2.89	73.48	0.00	0.18	0.00	0.00	0.02
Connective tissue	40	60	9.40	20.70	6.20	63.70	0.00	0.00	0.00	0.00	0.00
Skeletal tissue	60	220	9.63	46.17	2.48	35.74	0.00	1.94	0.00	0.00	4.05
Skeletal tissue	220	380	8.85	42.31	2.69	36.79	0.00	2.99	0.00	0.00	6.37
Skeletal tissue	380	540	8.14	38.84	2.89	37.73	0.00	3.93	0.00	0.00	8.46
Skeletal tissue	540	700	7.51	35.71	3.07	38.59	0.00	4.79	0.00	0.00	10.34
Skeletal tissue	700	860	6.93	32.88	3.22	39.36	0.00	5.56	0.00	0.00	12.05
Skeletal tissue	860	1020	6.41	30.29	3.37	40.07	0.00	6.27	0.00	0.00	13.60
Skeletal tissue	1020	1180	5.93	27.93	3.50	40.71	0.00	6.91	0.00	0.00	15.02
Skeletal tissue	1180	1340	5.48	25.76	3.62	41.30	0.00	7.50	0.00	0.00	16.33
Skeletal tissue	1340	1500	5.08	23.76	3.74	41.85	0.00	8.05	0.00	0.00	17.53
Skeletal tissue	1500	1660	4.70	21.91	3.84	42.35	0.00	8.55	0.00	0.00	18.64
Skeletal tissue	1660	1820	4.35	20.20	3.94	42.82	0.00	9.02	0.00	0.00	19.67
Skeletal tissue	1820	1980	4.03	18.60	4.03	43.25	0.00	9.45	0.00	0.00	20.63
Skeletal tissue	1980	2140	3.73	17.12	4.11	43.66	0.00	9.86	0.00	0.00	21.53
Skeletal tissue	2140	2300	3.45	15.73	4.19	44.04	0.00	10.24	0.00	0.00	22.36
Skeletal tissue	2300	2460	3.18	14.43	4.26	44.39	0.00	10.59	0.00	0.00	23.14
Skeletal tissue	2460	2620	2.94	13.21	4.33	44.72	0.00	10.92	0.00	0.00	23.88
Skeletal tissue	2620	2780	2.70	12.07	4.39	45.04	0.00	11.24	0.00	0.00	24.57
Skeletal tissue	2780	2940	2.48	10.99	4.45	45.33	0.00	11.53	0.00	0.00	25.22
Skeletal tissue	2940	3071	2.29	10.06	4.51	45.58	0.00	11.78	0.00	0.00	25.77

Table 3.3: **CT value to elemental composition as determined from the calibration with CIRS scanned by QuantumGx2.**

The Hounsfield Unit to elemental composition mapping consists of various step functions from HU value to abundance of atom types in the tissue. From each calibration set-up, a table is constructed converting HU values to elemental compositions yielding one region of HU values classified as air, one as lung, several as soft tissues, one as connective tissue, and several as skeletal tissues. The standard deviations of the measurements of surrogate phantom insert scans determine the size of the HU ranges, leading to more soft tissue and skeletal tissue regions after calibration with the QuantumGx2 (Tables 3.3 and A.2) than with the VECTor micro-CT scanner (Tables 3.4 and A.3).

Tissue	CT range (HU)		Elemental composition (%) H	C	N	O	Mg	P	Cl	Ar	Ca
Air	-1024	-950	0.00	0.00	75.50	23.20	0.00	0.00	0.00	1.30	0.00
Lung	-950	-189	10.30	10.50	3.10	75.90	0.00	0.20	0.00	0.00	0.00
Soft tissue	-189	-100	11.30	56.00	0.93	31.74	0.00	0.03	0.00	0.00	0.00
Soft tissue	-100	-32	10.80	36.35	2.12	50.67	0.00	0.08	0.00	0.00	0.00
Mix soft tissues	-32	40	10.34	13.08	2.89	73.48	0.00	0.18	0.00	0.00	0.02
Connective tissue	40	60	9.40	20.70	6.20	63.70	0.00	0.00	0.00	0.00	0.00
Skeletal tissue	60	230	10.16	48.79	2.33	35.02	0.00	1.22	0.00	0.00	2.47
Skeletal tissue	230	400	9.64	46.21	2.48	35.73	0.00	1.93	0.00	0.00	4.03
Skeletal tissue	400	570	9.15	43.80	2.61	36.38	0.00	2.58	0.00	0.00	5.47
Skeletal tissue	570	740	8.69	41.55	2.74	36.99	0.00	3.19	0.00	0.00	6.83
Skeletal tissue	740	910	8.27	39.45	2.86	37.57	0.00	3.77	0.00	0.00	8.09
Skeletal tissue	910	1080	7.86	37.47	2.97	38.11	0.00	4.31	0.00	0.00	9.28
Skeletal tissue	1080	1250	7.49	35.61	3.07	38.62	0.00	4.82	0.00	0.00	10.40
Skeletal tissue	1250	1420	7.13	33.85	3.17	39.09	0.00	5.29	0.00	0.00	11.46
Skeletal tissue	1420	1590	6.79	32.20	3.26	39.55	0.00	5.75	0.00	0.00	12.45
Skeletal tissue	1590	1760	6.48	30.64	3.35	39.97	0.00	6.17	0.00	0.00	13.39
Skeletal tissue	1760	1930	6.17	29.15	3.43	40.38	0.00	6.58	0.00	0.00	14.29
Skeletal tissue	1930	2100	5.89	27.75	3.51	40.76	0.00	6.96	0.00	0.00	15.13
Skeletal tissue	2100	2270	5.62	26.42	3.59	41.12	0.00	7.32	0.00	0.00	15.93
Skeletal tissue	2270	2440	5.36	25.15	3.66	41.47	0.00	7.67	0.00	0.00	16.70
Skeletal tissue	2440	2610	5.11	23.94	3.73	41.80	0.00	8.00	0.00	0.00	17.42
Skeletal tissue	2610	2780	4.88	22.79	3.79	42.11	0.00	8.31	0.00	0.00	18.12
Skeletal tissue	2780	2950	4.66	21.69	3.85	42.41	0.00	8.61	0.00	0.00	18.78
Skeletal tissue	2950	3071	4.47	20.79	3.90	42.66	0.00	8.86	0.00	0.00	19.32

Table 3.4: **CT value to elemental composition as determined from the calibration with CIRS scanned by VECTor.**

3.2.2. Validation via relative stopping power

The determined densities and elemental compositions from the CIRS and Gammex as determined from the measured HU values and the calibration curves should be validated via comparison of determined relative stopping power ratios with either measured SPRs or calculated SPRs.

The calibrated stopping powers from CIRS inserts mimic the actual stopping powers well (Fig. 3.4a). For the QuantumGx2 involved calibration, the relative deviations of stopping power do not exceed $\pm$2% for all CIRS inserts except for lung inserts (Fig. 3.4c). Stopping power ratios of lung inserts deviate with 7.1 and 10.4% from the real stopping power ratio. The deviations for stopping power ratios determined from VECTor-calibration are larger. The stopping power deviations from soft- and skeletal tissues do not exceed $\pm$6.5% and the lung inserts deviate with 6.6% and 10.6% from the actual stopping power.

In both cases, lung tissues were assigned much less carbon (≈ 60% to ≈10%) and much more oxygen (≈20% to ≈75%) than these inserts actually contain. This may induce the large variation in relative stopping power.

For the gammex inserts, stopping power predictions were less accurate with many stopping power deviations exceeding $\pm$5% (Fig. 3.4b,d). In general, the calibration with the QuantumGx2 scanner underestimated the stopping power of the inserts, while the calibration based on VECTor scans overestimated them. For both, lung tissues were assigned much less carbon than they actually contain. This may explain the larger deviations for lung tissues than other tissues.

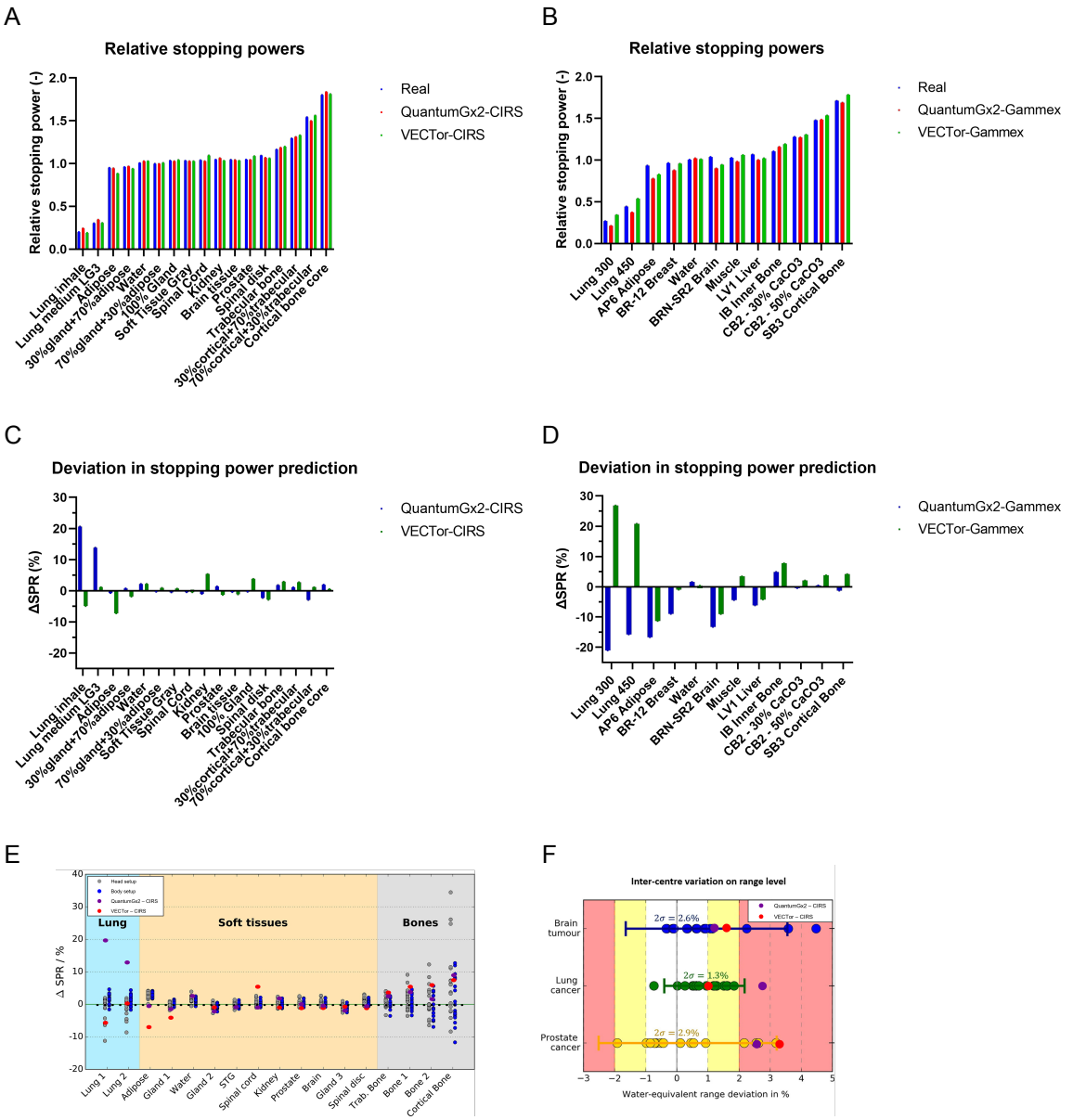

Figure 3.4: **Comparison between real, measured, and determined stopping power ratios for surrogate tissues.** The stopping power for CIRS (A) and Gammex (B) tissue surrogates as determined from the actual density and composition and from the chosen density and composition based on CT measurements and calibration. The relative deviation of calibration-determined stopping powers with respect to real stopping powers for CIRS (C) and Gammex (D). (E) Deviation in determined stopping power ratio and range compared to measurements of Peters et al. (F) and determined proton ranges in the head, thorax, and abdomen are compared with calculations from Peters et al.[52]

Besides comparison with calculated stopping power ratios, stopping power prediction of CIRS inserts was compared with measured stopping powers of Peters et al. and predictions made by other proton institutes collected by this paper [52]. Stopping powers predictions of lung tissues by both calibration methods had larger deviations than other centers (Fig. 3.4e). The stopping power predictions of soft and skeletal tissues were however quite accurate using both scanners. The calibration based on VECTor scans did yield some deviations for adipose, gland 1 and spinal cord inserts. Furthermore, the theoretical range for brain, lung, and prostate tumours were compared. Here both methods were within the standard deviation of the other centers for brain tumours, while only calibration based on VECTor scans was accurate for lung cancer, and only calibrations based on QuantumGx2 scans for prostate cancer (Fig. 3.4f). This results from the large deviations in SPR for lung tissues calibrated with QuantumGx2, and consistent minor errors for all soft tissues and bones for VECTor based calibration.

3.2.3. Validation via phantom irradiation

From the CT calibration and the Quantum Gx2 micro-CT scan of a real mouse, the expected proton range can be determined. Via ray tracing, energy loss of protons of 150 MeV interacted with the tissues in front of the tumour and the tumour was calculated and the range was determined. A mouse-like phantom was irradiated with RW3 slabs in front. The thickness of the RW3 slabs resulted from the subtraction of the proton range of 150 MeV protons in water by the calculated range in the mouse.

The design of the murinemorphic phantom contained soft tissues, bones, lungs, and a tumour within two insertable segments in the head (Fig. 3.5a). Although a margin of air was designed behind the four segments, the printed segments had to be polished to properly fit when inserting EBT3 gafchromic films. The 3D-printed phantom has soft tissues (white), bones (black), a tumour (transparent) and lungs (invisible on Fig. 3.5b). Micro-CT scans of the phantom and a test print were performed with the QuantumGx2 to assess contrast between the materials (Fig. 3.5c,d). This contrast is good for small structures, yet soft tissues in HIPS sometimes contain holes as seen in figure 3.5c, while the PLA (for bones) contains these air gaps in the test print (Fig. 3.5d). These air gaps both decrease contrast and may affect the interactions of the phantom with protons, since it decreases the average stopping power.

The density and water-equivalent thickness of 5x5x1 cm plates of HIPS and PLA were determined by Marta Rovituso (Holland PTC). The densities were 1.08 g/cm^3 and 1.17 g/cm^3 for HIPS and PLA respectively. The water equivalent materials were measured as 0.97 or both.

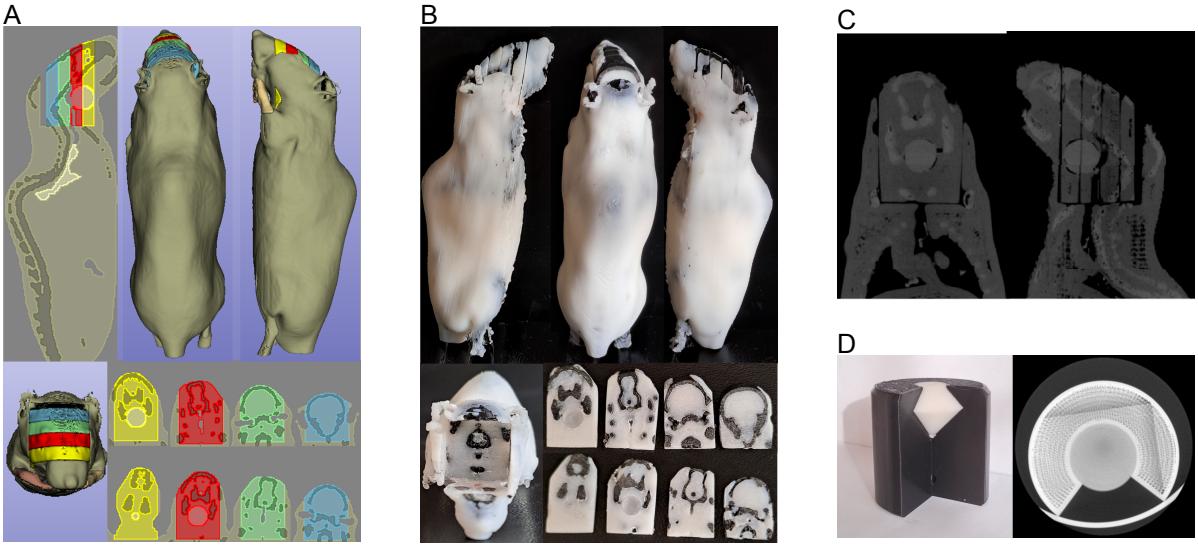

Figure 3.5: **Design and final murinemorphic mouse phantom.** (A) The design of the mouse phantom with different materials for soft tissue bones and lung, and four segments including a tumour. (B) The 3D-printed mouse phantom with removable inserts. (C) A micro-CT scan of the mouse phantom by the QuantumGx2 scanner. (D) Micro-CT scans of a test print with PLA (black) and HIPS (white) to assess the contrast during imaging.

Before irradiation of the phantom, EBT3 gafchromic films were irradiated with known doses and scanned (Fig. 3.6a). Since measured optical densities of the non-irradiated background films were almost equal (data not shown), the background signal was not subtracted from the irradiated signals, but taken along in the optical density to dose calibration.

The optical density to dose calibration curve was created using original films and films corrected for the lateral scan effect. Since the correction of the lateral scan effect is only valid until 5 Gy, films irradiated with higher doses were not taken into account. No major differences were observed for dose calibration curves with and without lateral scan effect correction, except for a trend towards saturation for corrected films at 5 Gy (Fig. 3.6b). Both datasets were fit to the theoretical optical density to dose conversion formula with R-squared of 0.9997 and higher.

The murinemorphic phantom including six EBT3 gafchromic films was irradiated with 5 Gy of protons (Fig. 3.6c). Since at the center of the film scanner no differences were observed between non-corrected and corrected films and the small films were scanned in another position of the scanner, the lateral scan effect was corrected. The optical density was converted to dose resulting in six dose distributions

visualised by film with a maximum detected dose of approximately 2 Gy (Fig. 3.6d). The dose of 5 Gy the phantom was irradiated with has not been reached. The dose drops further with distance and structures of the bones can be observed for films 3 and 4. The white horizontal line in film 6, placed behind the mouse, originates from the gap of air between the segments and the rest of the phantom. Since the protons travel through air they lose less energy leading to a high dose at the sixth position. The black piece below is positioned behind the thicker bulk of the phantom to which protons lose more energy.

Horizontal and vertical dose profiles confirm the decrease of dose over depth (Fig. 3.6e). These line profiles were positioned through the higher dose spot in films 3 and 4 and vertical dose profiles were taken on the symmetry line of each dose distribution (where possible). From each horizontal profile a homogeneous section of 0.40 cm was averaged, resulting in a dose profile over depth (Fig. 3.6f). Doses drop from ≈1.75 Gy to zero when reaching the fifth film positioned behind the fourth phantom segment. This distal fall-off is rapid, but the tumour has not been irradiated homogeneously.

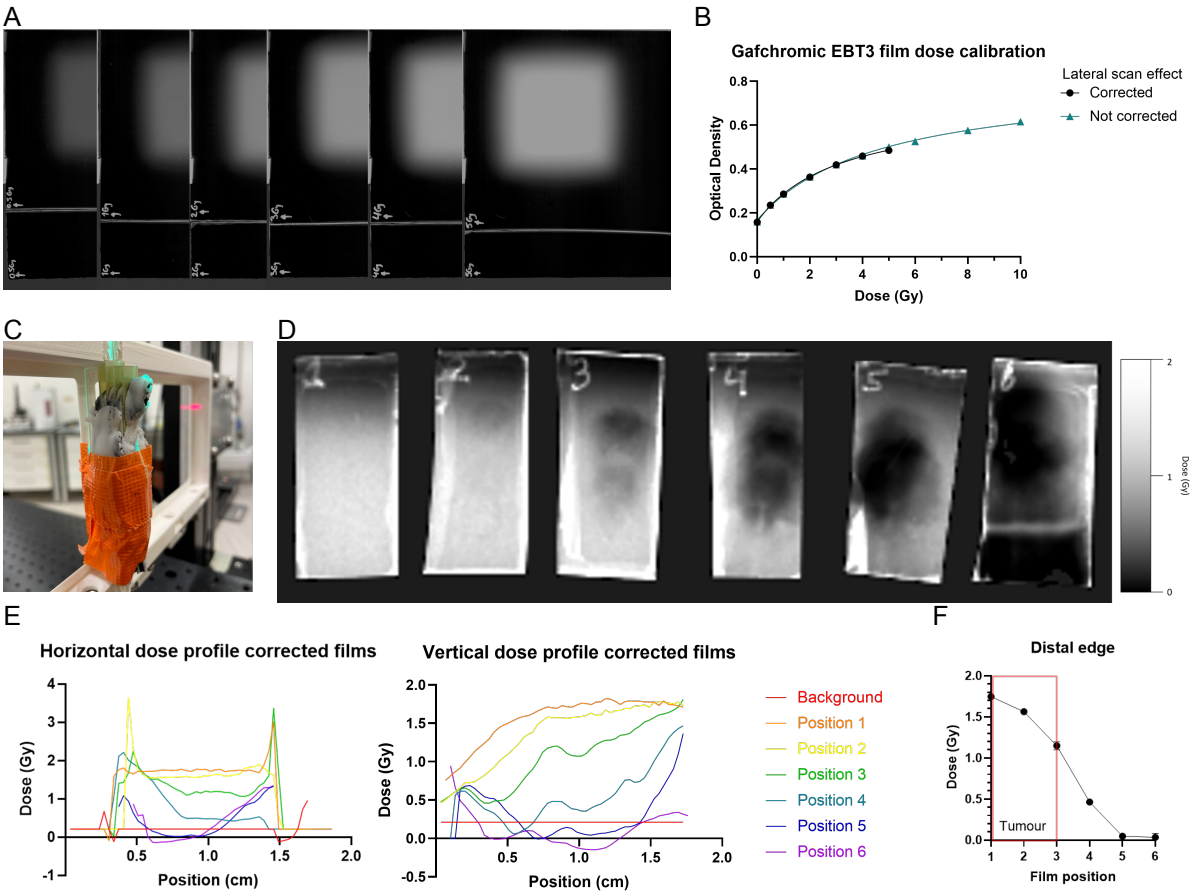

Figure 3.6: **Range and dose validation of a murinemorphic phantom irradiation.** (A) Irradiated films by known doses were used for optical density to dose calibration. (B) The effect of lateral scan effect correction on the optical density to dose curve. (C) EBT3 gafchromic films in the phantom were irradiated and (D) scanned to visualise the dose distributions. (E) Horizontal and vertical dose profiles of the films were taken and (F) the homogeneous regions are combined into a depth-dose curve.

The mouse irradiation was simulated in the Monte Carlo software program TOPAS [50]. A proton beam of 150 MeV was targeted to a micro-CT scan of a real mouse, traveling through the same beamline as in the physical experiment (Fig. 3.7a). The dose to medium was measured by an axial scorer through the collimator, Rw3 slabs, and mouse, and six lateral scorers mimicking the EBT3 films of the experimental irradiation. The relative dose profile shows major dose deposition in the collimator and narrowing of the proton beam, followed by a gradual increase in dose deposition in the RW3 slabs, and final stopping of protons (or scattering around) in the mouse (Fig. 3.7b). The dose profile at the center of the proton beam ($x = 0, y = 0$) confirms this pattern (Fig. 3.7c). Within the collimator strong dose deposition was observed. In the water-equivalent RW3 slabs, the depth-dose curve is highly similar to the spread-

out Bragg peak. Therefore, the mouse is positioned within the distal edge, leaving just some minor dose deposition. A zoom-in into this region is shown in figure 3.7d. The dose within the tumour is not homogeneous and the dose drops off rapidly in and behind the tumour. The latter is confirmed by lateral dose distributions measured by dose-to-medium scorers perpendicular to the beam line (Fig. 3.7e). The dose is high on films 1 and 2, but falls off rapidly afterwards. In film 4 some dose deposition is detected at the sides, which may be just outside of the mouse next to its neck. In general the dose distributions are noisy even though 30 million proton were ejected and detectors had thicknesses of 1 mm allowing them to detect more particles. In these films no anatomical structures can be resolved as was possible in physical films shown in figure 3.6d.

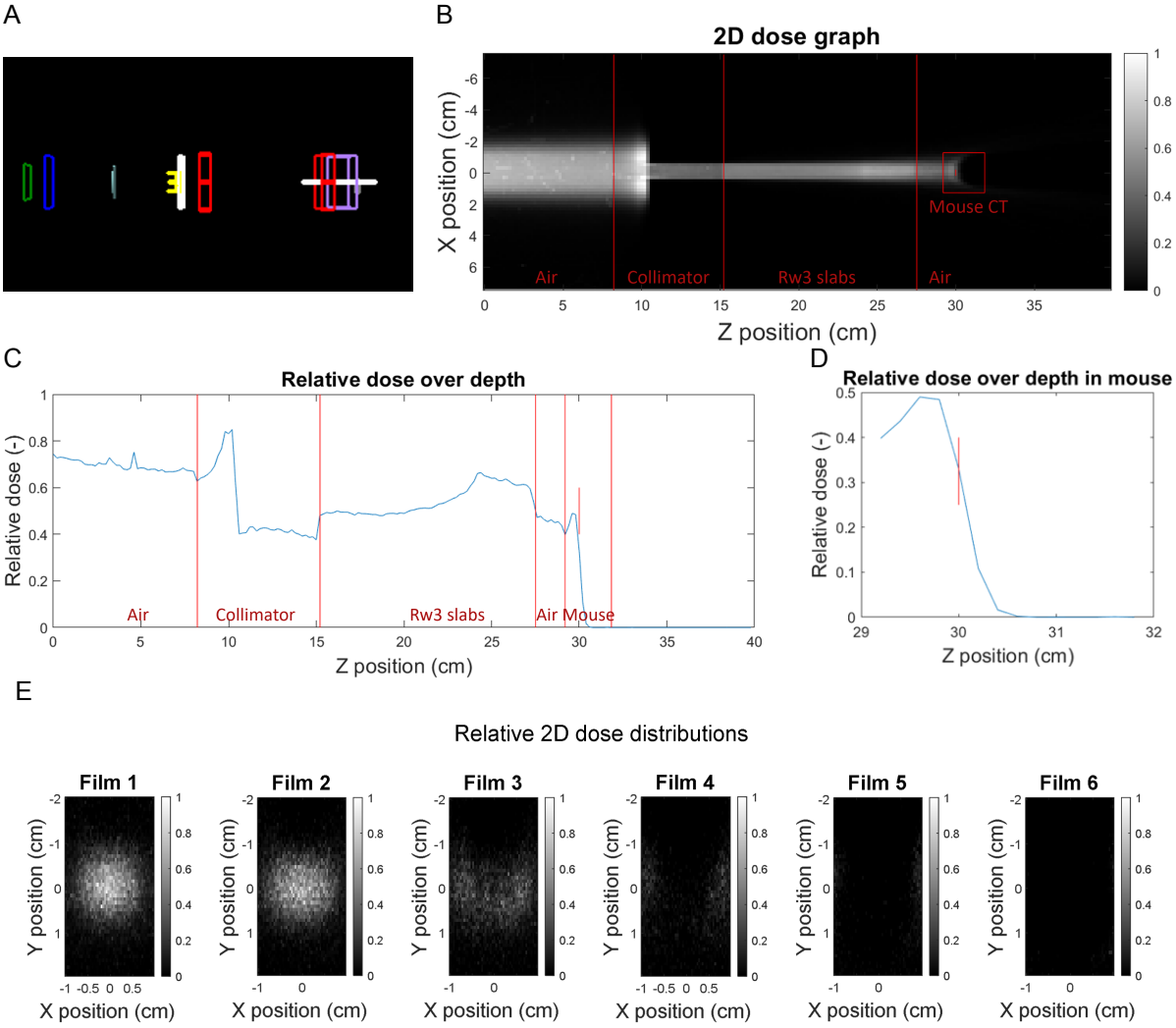

Figure 3.7: **Monte Carlo simulation of mouse proton irradiation.** (A) The beamline of the irradiation with the exit window (green), beam monitor (blue), dual ring (gray), ridge filter (yellow), collimators (red), RW3 slabs (purple), mouse CT scan (gray), and scorers (white). (B) The 2D dose graph detected by the axial scorer through collimator, Rw3 slabs and mouse and (C) its profile through the center. (D) The relative dose over depth within the mouse CT scan region. In figures b, c, and d a small red line denotes the center of the tumour. (E) The 2D dose graphs at the positions of lateral scorers mimicking EBT3 films.

Range estimation performed by CT calibration of QuantumGx2 mouse scans resulted in a proton range close to the end of the tumour. Yet, the tumour has been irradiated by distal edge protons in both the experimental and Monte Carlo irradiation. This resulted in a rapid dose decrease in the tumour, failing to irradiate the tumour homogeneously. To reach a homogeneous dose in the tumour, the tumour should be placed in the spread-out Bragg peak.

3.3. Proton FLASH irradiations

Irradiation of biological tissues with varying radiation types may yield different results. Cells, for example, need lower doses of proton irradiation than x-ray irradiation to reach the same effect due to proton's higher LET in the Bragg peak. Furthermore, the proton dose rate tissues are irradiated with may affect the biological outcome due to the FLASH effect [26]. Here it is investigated whether differences in clonogenic survival are observed for varying radiation types and dose rates.

Both U2OS and FaDu cells had been irradiated by 0, 2, 4, or 6 Gy x-ray irradiation. This experiment was executed twice leading to similar results (Fig. 3.8a and Fig. A.6a). The clonogenic survival decreases with increasing dose, and U2OS cells were shown to be slightly more sensitive to x-ray irradiation. It should however be noted that the plating efficiency of FaDu cells was significantly smaller than for U2OS cells, which could have affected the survival rates.

The proton irradiations had only been performed for the head and neck squamous cell carcinoma derived FaDu cell line. The cells were irradiated with 0, 2, 4, or 6 Gy protons in two different set-ups. Set-ups including a thick scattering ring resulted in proton dose rates of approximately 1.5 Gy/min, while irradiations with the thin scattering ring reached dose rates of approximately 10 Gy/min. This experiment was performed under different conditions: the first time cells were irradiated dry (Fig. A.6b), afterwards cells were irradiated fully covered by medium. From the second experiment no results could be gathered due to cyclotron instability, but from the third experiment results were received (Fig 3.8b). The small difference in dose rates does not have any effect on the clonogenic survival of irradiated FaDu cells.

Although small deviations in dose rates do not affect clonogenic survival, large dose rates deviations may induce differences due to potential presence of the FLASH effect. Therefore, two experiments were performed with the thin ring set-up used previously as control and FLASH irradiations as set-up of interest. The second experiments experienced contaminations, but results from the first experiment were received successfully (Fig. 3.8c). The clonogenic survival curves do not fit the linear-quadratic model nor follow exponential like behaviours. No conclusions can be drawn from these results.

Investigation of the effect of proton dose rates on clonogenic survival of FaDu cells shows that minor dose rate deviations between 1.5 Gy/min and 10 Gy/min do not have an effect, while an effect of ultra-high dose rates can not be proven nor rejected.

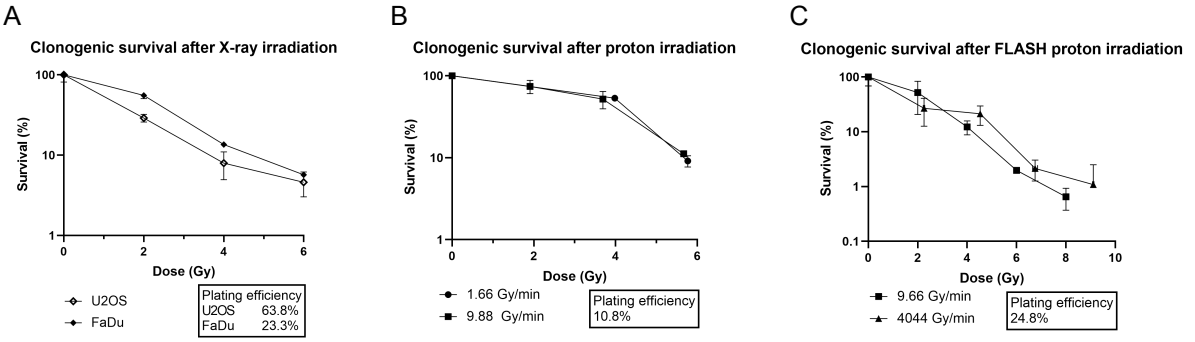

Figure 3.8: **Effect of different irradiation modalities on clonogenic survival.** (A) Clonogenic survival for U2OS and FaDu cells after x-ray irradiation. (B) Clonogenic survival of FaDu cells after proton irradiations with two low dose rates. The set-up reaching 10 Gy/min was used as control for (C) clonogenic survival of FaDu cells after conventional and FLASH proton irradiations.

4

Discussion

Radiosensitisation by DNA damage repair inhibition
Investigation of the DNA damage repair after x-ray and proton irritations was assessed by inhibition of repair pathways. The small-molecule inhibitor AZD7648 was supplemented to cells to inhibit non-homologous end-joining. AZD7648 was shown to inhibit phosphorylation of DNA-PKcs effectively and induced a radiosensitising effect on FaDu cells during x-ray irradiations. The efficacy of B02 to inhibit homologous recombination could not be proven and the component had no effect on clonogenic survival of FaDu cells during x-ray irradiations. Conclusions about the effects of AZD7648 and B02 on FaDu survival after proton irradiations could not be made.

These results imply that DNA damage induced by x-ray irradiation is (partly) repaired by non-homologous end-joining. Based on this, in the future patients with NHEJ deficient tumours may benefit from x-ray irradiations and could be selected for this treatment type. Besides this, AZD7648 could be investigated further in vivo to assess its safety and efficacy of radiosensitisation to become a potential drug in combination therapies with radiotherapy.

Some remarks about this project should be made. For example, the FaDu cell line has a insertion at position 32911073 of glutamine leading to a frame shift in the BRCA2 gene [53]. Therefore, homologous recombination may be compromised already. Yet, since the allelic fraction of this insert is only $1.65 \cdot 10^{-}5$, the effect on homologous recombination in our FaDu cells should be limited.

Although B02 was shown to inhibit homologous recombination effectively by Huang et al. [18], this was not confirmed in the thesis. Huang et al. performed a similar flow-cytometry based traffic light reporter assay showing a decrease in GFP signal upon B02 addition, indicating inhibition of homologous recombination. They furthermore showed decreasing presence of the Rad51-ssDNA complex upon incubation with B02 via electrophoretic mobility shift assays. The compound B02 thus successfully inhibited homologous recombination by blocking binding of Rad51 to single-stranded DNA. We may perform the latter assay as well to investigate HR inhibition by B02 and its potential radiosensitising effect.

Alternatives for homologous recombination inhibition by small-molecules are for example imatinib which reduces Rad51 expression [54], BRD inhibitors [55], or 35d which blocks interactions between Rad51 and BRCA2 [56]. Even if these small molecules inhibit homologous recombination effectively, administration to patient tumours only will be difficult. Therefore,currently most research regarding homologous recombination inhibition is based on mild hyperthermia. This effectively inhibits homologous recombination and can be applied locally [57].

Small-animal proton dosimetry
In the second project a dosimetric validation of mouse proton irradiations was performed to determine proton range in small-animals. CT calibrations mapping Hounsfield units to proton stopping power ratios are performed regularly in the clinic, yet this thesis is (one of) the first applying this for pre-clinical micro-CT scanners. Stopping powers determined for CIRS phantom inserts were accurate and a mouse-like phantom was irradiated with protons of the distal edge of the Bragg curve. This method with some improvements will allow for many in vivo experiments dependent on comparisons of healthy and tumour tissues. Therefore, this will be a stepping stone for in vivo research on proton therapy.

Regarding the dosimetry for small animal proton irradiations, multiple improvements are possible and remarks should be made. In this thesis, resemblance between biological tissues and the surrogate tissues of the CIRS and Gammex phantom was shown using mass density and effective atomic number information. Here, the most common approach to calculate the effective atomic number Z_{eff} from Mayneord was used [58], who derived this approach from attenuation measurements of materials using low energy photons. However, the effective atomic number was shown to be highly energy dependent, as for example the effective atomic number of water is ≈6.1 using 10 keV photons, but ≈3.4 using 100 keV photons [59]. Note that this is a large difference considering that water is mainly composed of hydrogen ($Z = 1$) and oxygen ($Z = 8$). Taylor et al. created a software program which determines the effective atomic number for user specified materials and photon energy spectra using the cross section of the atoms [60]. With this it takes into account the energy-dependent interactions between photons and the material like photoelectric effect, (in)coherent scattering, and pair and triplet production. A recent paper continues on this work, creating a software package in which effective atomic numbers can be determined for photon, proton, and charged particle irradiations [61]. Although this would highly improve the calculation of effective atomic number, it should be noted that this parameter has purely be shown in this thesis, but not used in the Hounsfield Units to stopping power ratio calibration.

The surrogate tissues from Gammex and CIRS are equivalent to human biological tissues. Besides this, the density and elemental composition of the 71 biological tissues used during CT calibration were human as well. This data is not yet present for animal models, but ICRP has recommended that for all reference animals and plants the elemental composition of various tissues should be determined [62].

The CT scans acquired by the QuantumGx2 scanner have little noise and low standard deviations. Yet, low Hounsfield unit regions at the center of the image were observed. In general, the image's center is more susceptible to defective pixels of which the effect on the reconstructed image can be reduced by gain calibration [63].

The CT scans acquired by the VECTor scanner were noisy and resulted in large standard deviations. Improvements can be made during reconstruction with a Ram-Lak filter as used for the QuantumGX2, after reconstruction with an extra filter, and by performing binning to remove some noise [64]. In general, image acquisition and reconstruction should be performed with a higher resolution than required. The required resolution will be achieved afterwards via binning. Furthermore, the physical filter of aluminium and copper is not available in Erasmuc MC's VECTor scanner, but can be used for experiments at MILabs. This would remove some beam hardening artefacts. This will be performed in the follow-up project by Michèle Knol.

The inserts of the QuantumGx2 and VECTor mimic the size of a mouse instead of the size of the individual organs. Therefore, higher voltages are necessary for image acquisition of these inserts than for mice. A resin cylinder of 32 mm in diameter and 40.4 mm in height containing five rods of varying calcium hydroxyapatite concentration can be used as representative for bone tissues [65]. If data on the exact elemental composition of these rods can be acquired, inclusion of these rods in the CT calibration will be an improvement. Small phantoms of tissue-equivalent materials including lungs and soft tissues also exist, yet none was found with multiple lung tissues, soft tissues, and skeletal tissues.

The CT calibration of Schneider et al. [36] was chosen since stoiciometric methods taking material propoerties into account were shown to be more accurate than empiric methods linking HU values to SPR directly [52] and since this could be implemented in the Monte Carlo simulation software TOPAS allowing for in silico validation. Yet, instead of Schneider's method other methods could be used as well. Taasti et al. created an accurate method linking HU values to stopping power ratios directly using dual-energy CT scanners [66]. Although our CT calibration was intended for monoenergetic CT scanners, two scans acquired with different energies can be summed and used as if acquired by a dual-energy CT scanner.

During the CT calibration, two CT scanner specific parameters are fitted describing interactions between photons and the inserts. Least square fitting did result in small errors, but the values of the parameters could not be interpreted nor compared. This is caused by the fact that the fits led to local minima. Improvement of the fitting strategy to reach the global minima, may result in more interpretative values for the two parameters since this limits the effect of randomness in the fitting iterations.

The stopping power calibration for CIRS yielded acceptable results. The determined stopping powers had small deviations with calculated stopping powers. Furthermore, the deviations are comparable with stopping power ratio deviations reached by other institutes using clinical CT scanners as summarised by Peters et al. [52] However, the calibrations with both scanners for Gammex inserts was

off. A clear explanation of this could not be found. Both the determined densities and elemental compositions are close to the actual properties. Here, carbon and oxygen are an exception with large differences in percentages.Yet this is the case for the CIRS calibrations as well, where accurate results were reached. Besides this, it was discussed whether the difference in amount of inserts (16 for CIRS, 11 for gammex) could explain this. This may also not be true, since the eventual calibration curves are based on the same 71 biological tissues for both.

Validation of the range was performed by irradiation of a mouse phantom and detection of the doses inside the phantom. It should be mentioned that the materials the phantom is composed of are similar to biological tissues in mass densities, but elemental compositions are unknown. Furthermore, small airgaps between the printed layers were observed in CT scans of the printed phantom. This can be avoided by the use of a smaller printing nozzle to reach thinner layers [67]. Furthermore, the material HIPS (used for soft tissue and tumour) is known for splitting of its layers, called delamination. This can be prevented by printing with a higher temperature to increase the bond's strength between the layers [68].

At last, EBT3 films irradiated with 10x10 cm fields of known doses were scanned in the center of the film scanner while EBT3 films irradiated within the mouse phantom were scanner in the upper-left corner. Due to the lateral scan effect, a choice was made to align all upper-left corners with a frame to allow for easy position determination. However, the lateral scan effect has limited effect on the center of the scanner, but up to 3% reduction of optical density at the left side [69]. Therefore it is recommended to position all films in the center of the scanner to limit the influence of the lateral scan effect.

Proton FLASH irradiations

At last, proton irradiations at ultra-high dose rates were performed to potentially induce a FLASH effect in FaDu cells. A significant difference has not been observed on the clonogenic survival of FaDu cells between conventional and FLASH irradiated cells. No difference in clonogenic survival after proton irradiations with small variations in dose-rates were reported. The observed induction of the FLASH effect in FaDu cells would have boosted research regarding the biological mechanism of the FLASH effect. Unfortunately, this research has not contributed to this goal.

Clear conclusions from the FLASH experiments on FaDu cells cannot be drawn due to the large standard deviations in the data. This was (partly) caused by the low amount of cells irradiated in the 24 well plates. These 24 well plates should be used during irradiation due to the limited field size of the FLASH proton beam, however other assays require less cells than clonogenic survivals. For example, cells can be irradiated and stained for 53BP1 and RPA after varying timepoints. These fluorescently labeled double stranded break markers can be visualised during fluorescence confocal imaging in which only tens to hundreds of cells are required. This will not result in a comparison between survival of FaDu cells after conventional and FLASH irradiations, but it may provide information on the extent of DNA damage induced by these types of irradiations.

Furthermore, a review of Vozenin et al. gathering in vitro FLASH results showed that FLASH effects had not been observed at normoxic oxygen concentrations (21%) but only at lower oxygen concentrations [70]. Since oxygen is thought to play a role in the biological mechanism of FLASH via oxygen depletion or the generation of reactive oxygen species, performing in vitro experiments at oxygen concentration similar as for biological tissues is crucial. Instead, experiments should be performed at physoxic oxygen concentrations between 3% and 7.4% for different tissues [71]. To expand on this, oxygen affects the response to radiation in general. So whenever oxygen concentrations have been decreased for the FLASH experiments, this can be used for the x-ray and proton experiments investigating DNA damage repair inhibition as well.

5

Conclusion

In this thesis, multiple improvements of proton therapy were investigated. The necessity of two DNA damage repair pathways were analysed after X-ray and proton irradiations. Inhibition of the DNA repair pathway repairing the radiation induced damage may lead to radiosensitisation. It was shown that the small-molecule inhibitor effectively inhibits phosphorylation of DNA-PKcs on the Ser2056 site and has a radiosensitising effect on FaDu cells irradiated by X-rays. No conclusions can be drawn for the effect on FaDu cells during proton irradiations. Efficacy of the small-molecule inhibitor B02 on homologous recombination could not be proven. B02 was shown to have no effect on FaDu cells irradiation with x-rays, but conclusions from proton irradiations could not be drawn.

Next, a dosimetry pipeline for small-animal irradiations was presented and validated. Here micro-CT calibration from Hounsfield Unit to stopping power was executed with two different scanners in combination with insert from two different tissue-equivalent phantoms. Even though scanner specifics should be corrected for with two fitting parameters, the abundance of contrast and noise in the CT images still affects the stopping power calibrations. Eventually, methods involving QuantumGx2 or VECTor with CIRS inserts resulted in small deviations in determined stopping power ratios, with the exception for lung tissues. Using Gammex inserts, a lower accuracy in stopping power calibration was achieved. The range was validated for old results of the QuantumGx2-CIRS stopping power calibration by irradiation of a murinemorphic phantom. The measured dose distributions on films at multiple depths showed that the tumour was irradiated with protons from the end of the spread-out Bragg peak or even distal edge. This was confirmed by Monte Carlo simulations.

At last, the effect of proton dose rates on clonogenic survival of FaDu cells was assessed. Small differences in low dose rates do not affect its survival. A comparison between conventional and FLASH dose rates could not be made due to large standard deviations. A FLASH effect induced in FaDu cells could thus not be proved nor rejected.

Bibliography

[1] International Agency for Research on Cancer. Estimated number of new cases in 2020, worldwide, both sexes, all ages (excl. nmsc). URL `https://gco.iarc.fr/today/online-analysis-table`.

[2] R.L. Siegel, K.D. Miller, H.E. Fuchs, and A. Jemal. Cancer statistics, 2021. *Cancer Statistics*, 71: 7–33, 2021.

[3] P. Strojan, K. A. Hutcheson, A. Eisbruch, J. J. Beitler, J. A. Langendijk, A. W. M. Lee, J. Corry, W. M. Mendenhall, R. Smee, A. Rinaldo, and A. Ferlito. Treatment of late sequelae after radiotherapy for head and neck cancer. *Cancer treatment review*, 59:79–92, 2017.

[4] H. Paganetti, C. Beltran, S. Both, L. Dong, J. Flanz, K. Furutani, C. Grassberger, D. R. Grosshans, A. C. Knopf, J. A. Langendijk, H. Nystrom, K. Parodi, B. W. Raaymakers, C. Richter, G. O. Sawakuchi, M. Schippers, S. F. Shaitelman, B. K. K. Teo, J. Unkelback, P. Wohlfahrt, and T. Lomax. Roadmap: proton therapy physics and biology. *Physics in Medicine Biology*, 66, 2021.

[5] A. Jakobi, A. Bandurska-Luque, K. Stützer, R. Haase, S. Löck, L. J. Wack, D. Mönnich, D. Thorwarth, D. Perez, A. Lühr, D. Zips, M. Krause, M. Baumann, R. Perrin, and C. Richter. Identification of patient benefit from proton therapy for advanced head and neck cancer patients based on individual and subgroup normal tissue complication probability analysis. *International Journal of Radiation Oncology* Biology*, 92:1165–1174, 2015.

[6] Brita Singers Sørensen, Jens Overgaard, and Niels Bassler. In vitro rbe-let dependence for multiple particle types. *Acta oncologica*, 50(6):757–762, 2011.

[7] Taeko Matsuura, Yusuke Egashira, Teiji Nishio, Yoshitaka Matsumoto, Mami Wada, Sachiko Koike, Yoshiya Furusawa, Ryosuke Kohno, Shie Nishioka, Satoru Kameoka, Katsuya Tsuchihara, Mitsuhiko Kawashima, and Takashi Ogino. Apparent absence of a proton beam dose rate effect and possible differences in rbe between bragg peak and plateau. *Medical Physics*, 37:5376–5381, 2010.

[8] A. O. Fontana, M. A. Augsburger, N. Grosse, M. Guckenberger, A. J. Lomax, A. A. Sartori, and M. N. Pruschy. Differential dna repair pathway choice in cancer cells after proton-and photon-irradiation. *Radiotherapy and Oncology*, 116:374–380, 2015.

[9] N. Grosse, A. O. Fontana, E. B. Hug, A. Lomax, A. Coray, M. Augsburger, H. Paganetti, A. A. Sartori, and M. Pruschy. Deficiency in homologous recombination renders mammalian cells more sensitive to proton versus photon irradiation. *International Journal of Radiation Oncology*, 88: 175–181, 2014.

[10] K. Szymonowicz, A. Krysztofiak, J. Van der Linder, A. Kern, S. Deycmar, S. Oeck, A. Squire, B. Koska, J. Klouschek, M. Vüllings, C. Neander, J. T. Siveke, J. Matschke, M. Pruschy, B. Timmerman, and V. Jendrossek. Proton irradiation increases the necessity for homologous recombination repair along with the indispensability of non-homologous end joining. *Cells*, 9:889, 2020.

[11] James M Daley, Hengyao Niu, Adam S Miller, and Patrick Sung. Biochemical mechanism of dsb end resection and its regulation. *DNA repair*, 32:66–74, 2015.

[12] Naoya Uematsu, Eric Weterings, Ken-ichi Yano, Keiko Morotomi-Yano, Burkhard Jakob, Gisela Taucher-Scholz, Pierre-Olivier Mari, Dik C Van Gent, Benjamin PC Chen, and David J Chen. Autophosphorylation of dna-pkcs regulates its dynamics at dna double-strand breaks. *The Journal of cell biology*, 177(2):219–229, 2007.

[13] Bailin Zhao, Eli Rothenberg, Dale A Ramsden, and Michael R Lieber. The molecular basis and disease relevance of non-homologous dna end joining. *Nature Reviews Molecular Cell Biology*, 21(12):765–781, 2020.

[14] William Douglass Wright, Shanaya Shital Shah, and Wolf-Dietrich Heyer. Homologous recombination and the repair of dna double-strand breaks. *Journal of Biological Chemistry*, 293(27): 10524–10535, 2018.

[15] J Brooks Crickard, Corentin J Moevus, Youngho Kwon, Patrick Sung, and Eric C Greene. Rad54 drives atp hydrolysis-dependent dna sequence alignment during homologous recombination. *Cell*, 181(6):1380–1394, 2020.

[16] Gerarda van de Kamp, Tim Heemskerk, Roland Kanaar, and Jeroen Essers. Dna double strand break repair pathways in response to different types of ionizing radiation. *Frontiers in Genetics*, 12, 2021.

[17] Jacqueline H.L. Fok, Antonio Ramos-Montoya, Mercedes Vazquez-Chantada, Paul W.G. Wijnhoven, Valeria Follia, Neil James, Paul M. Farrington, Ankur Karmokar, Sophie E. Willis, Jonathan Cairns, Jenni Nikkilä, David Beattie, Gillian M. Lamont, M. Raymond V. Finlay, Joanne Wilson, Aaron Smith, Lenka Oplustil O'Connor, Stephanie Ling, Stephen E. Fawell, Mark J. O'Connor, Simon J. Hollingsworth, Emma Dean, Frederick W. Goldberg, Barry R. Davies, and Elaine B. Cadogan. Azd7648 is a potent and selective dna-pk inhibitor that enhances radiation, chemotherapy and olaparib activity. *Nature Communications*, 10, 12 2019. ISSN 20411723. doi: 10.1038/s41467-019-12836-9.

[18] Fei Huang, Olga M. Mazina, Isaac J. Zentner, Simon Cocklin, and Alexander V. Mazin. Inhibition of homologous recombination in human cells by targeting rad51 recombinase. *Journal of Medicinal Chemistry*, 55:3011–3020, 4 2012. ISSN 00222623. doi: 10.1021/jm201173g.

[19] J. Coderre. Radiation interactions with matter: energy deposition., 2014.

[20] George C. Kagadis Andrew Webb. *Introduction to biomedical imaging*. John Wiley & Sons, 2003. ISBN 978-0471237662.

[21] Lee A Feldkamp, Lloyd C Davis, and James W Kress. Practical cone-beam algorithm. *Josa a*, 1 (6):612–619, 1984.

[22] Gruetter Rolf. Fundamentals of biomedical imaging course slides, 2017.

[23] Samuel España and Harald Paganetti. The impact of uncertainties in the ct conversion algorithm when predicting proton beam ranges in patients from dose and pet-activity distributions. *Physics in Medicine & Biology*, 55(24):7557, 2010.

[24] Nils Peters, Patrick Wohlfahrt, Christina V. Dahlgren, Ludovic de Marzi, Malte Ellerbrock, Francesco Fracchiolla, Jeffrey Free, Carles Gomà, Joanna Góra, Maria F. Jensen, Tomasz Kajdrowicz, Ranald Mackay, Silvia Molinelli, Ilaria Rinaldi, Vasilis Rompokos, Dorota Siewert, Pieternel van der Tol, Xavier Vermeren, Håkan Nyström, Antony Lomax, and Christian Richter. Experimental assessment of inter-centre variation in stopping-power and range prediction in particle therapy. *Radiotherapy and Oncology*, 163:7–13, 10 2021. ISSN 18790887. doi: 10.1016/j.radonc.2021.07.019.

[25] R. J. Berry, E. J. Hall, D. W. Forster, T. H. Storr, and M. J. Goodman. Survival of mammalian cells exposed to x rays at ultra-high dose-rates. *The British Journal of Radiology*, 42:102–107, 1969.

[26] Vincent Favaudon, Laura Caplier, Virginie Monceau, Frédéric Pouzoulet, Mano Sayarath, Charles Fouillade, Marie-France Poupon, Isabel Brito, Philippe Hupé, Jean Bourhis, Janet Hall, Jean-Jacques Fontaine, and Marie-Catherine Vozenin. Ultrahigh dose-rate flash irradiation increases the differential response between normal and tumor tissue in mice. *Science translational medicine*, 6, 2014.

[27] E. Abel, S. Girdhani, I. Jackson, J. Eley, A. Katsis, A. Marschall, A. Rodriquez, S. Senapati, S. M. Bentzen, Z. Vujaskovic, R. Dua, and R. Parry. Characterization of radiation-induced lung fibrosis and mode of cell death using single and multi-pulsed proton flash irradiation. *International Journal of Radiation Oncology, Biology, Physics*, 105:E652–E653, 2019. doi: https://doi.org/10.1016/j.ijrobp.2019.06.1033.

[28] Brita Singers Sørensen, Mateusz Krzysztof Sitarz, Christina Ankjærgaard, Jacob G Johansen, Claus E Andersen, Eleni Kanouta, Cai Grau, and Per Poulsen. Pencil beam scanning proton flash maintains tumor control while normal tissue damage is reduced in a mouse model. *Radiotherapy and Oncology*, 2022.

[29] M. C. Vozenin, J. H. Hendry, and C. L. Limoli. Biological benefits of ultra-high dose rate flash radiotherapy: Sleeping beauty awoken. *Clinical Oncology*, 31:407–415, 7 2019. ISSN 14332981. doi: 10.1016/j.clon.2019.04.001.

[30] Jean Bourhis, Wendy Jeanneret Sozzi, Patrik Gonçalves Jorge, Olivier Gaide, Claude Bailat, Fréderic Duclos, David Patin, Mahmut Ozsahin, François Bochud, Jean-François Germond, et al. Treatment of a first patient with flash-radiotherapy. *Radiotherapy and oncology*, 139:18–22, 2019.

[31] J. Breneman. Implementation and conduct of the first in-human trial of flash radiotherapy. *Physica Medica*, 94S1:S3–S4, 2022.

[32] Pierre Montay-Gruel, Munjal M Acharya, Kristoffer Petersson, Leila Alikhani, Chakradhar Yakkala, Barrett D Allen, Jonathan Ollivier, Benoit Petit, Patrik Gonçalves Jorge, Amber R Syage, et al. Long-term neurocognitive benefits of flash radiotherapy driven by reduced reactive oxygen species. *Proceedings of the National Academy of Sciences*, 116(22):10943–10951, 2019.

[33] Xu Cao, Rongxiao Zhang, Tatiana V. Esipova, Srinivasa Rao Allu, Ramish Ashraf, Mahbubur Rahman, Jason R. Gunn, Petr Bruza, David J. Gladstone, Benjamin B. Williams, Harold M. Swartz, P. Jack Hoopes, Sergei A. Vinogradov, and Brian W. Pogue. Quantification of oxygen depletion during flash irradiation in vitro and in vivo. *International Journal of Radiation Oncology Biology Physics*, 111:240–248, 9 2021. ISSN 1879355X. doi: 10.1016/j.ijrobp.2021.03.056.

[34] Oliver H Lowry. Protein measurement with the folin phenol reagent. *J biol Chem*, 193:265–275, 1951.

[35] Kosuke Yusa, Liqin Zhou, Meng Amy Li, Allan Bradley, and Nancy L Craig. A hyperactive piggybac transposase for mammalian applications. *Proceedings of the National Academy of Sciences*, 108 (4):1531–1536, 2011.

[36] Wilfried Schneider, Thomas Bortfeld, and Wolfgang Schlegel. Correlation between ct numbers and tissue parameters needed for monte carlo simulations of clinical dose distributions. *Physics in Medicine & Biology*, 45(2):459, 2000.

[37] RA Rutherford, BR Pullan, and I Isherwood. Measurement of effective atomic number and electron density using an emi scanner. *Neuroradiology*, 11(1):15–21, 1976.

[38] DR White, HQ Woodard, and SM Hammond. Average soft-tissue and bone models for use in radiation dosimetry. *The British journal of radiology*, 60(717):907–913, 1987.

[39] HQ Woodard and DR White. The composition of body tissues. *The British journal of radiology*, 59 (708):1209–1218, 1986.

[40] Gammex. Tissue characterization gammex phantom model 467 user's guide.

[41] CIRS. Tissue-equivalent materials elemental composition data sheet: Cirs project 1744-00, 2020.

[42] Gafchromic. Gafchromic ™ dosimetry media, type ebt-3. URL www.FilmQAPro.com.

[43] The Math Works Inc. Matlab, 2020.

[44] A. Fedorov, R. Beichel, J. Kalpathy-Cramer, J. Finet, J. C. Fillion-Robin, S. Pujol, C. Bauer, D. Jennings, F. Fennessy, M. Sonka, J. Buatti, S. Aylward, J. V. Miller, S. Pieper, and R. Kikinis. 3d slicer as an image computing platform for the quantitative imaging network. *Magnetic Resonance Imaging*, 30:1323–1341, 2012.

[45] Slicer.org. 3d slicer, 2021.

[46] Wouter Crijns, Frederik Maes, UA Van Der Heide, and Frank Van den Heuvel. Calibrating page sized gafchromic ebt3 films. *Medical physics*, 40(1):012102, 2013.

[47] Wayne S Rasband. Imagej, us national institutes of health, bethesda, maryland, usa. *http://imagej. nih. gov/ij/*, 2011.

[48] M. Rituerto Prieto. Passive beam field characterization for application in radiobiology. Master's thesis, Delft University of Technology, 2020.

[49] A E Meijer. Back to the future towards ridge filters in clinical flash proton therapy treatment planning for neuro-oncological targets, 2021.

[50] J. Perl, J. Shin, J. Schümann, B. Faddegon, and H. Paganetti. Topas: An innovative proton monte carlo platform for research and clinical applications. *Medical Physics*, 39:6818–6837, 2012. ISSN 00942405. doi: 10.1118/1.4758060.

[51] Wilfried Schneider, Thomas Bortfeld, and Wolfgang Schlegel. Correlation between ct numbers and tissue parameters needed for monte carlo simulations of clinical dose distributions, 2000.

[52] Nils Peters, Patrick Wohlfahrt, Christina V Dahlgren, Ludovic de Marzi, Malte Ellerbrock, Francesco Fracchiolla, Jeffrey Free, Carles Gomà, Joanna Góra, Maria F Jensen, et al. Experimental assessment of inter-centre variation in stopping-power and range prediction in particle therapy. *Radiotherapy and Oncology*, 163:7–13, 2021.

[53] Depmap portal. Fadu. `https://depmap.org/portal/cell_line/ACH-000846?tab=mutation`, Accessed 12 October 2022.

[54] Ananya Choudhury, Helen Zhao, Farid Jalali, Shahnaz Al Rashid, Jane Ran, Stephane Supiot, Anne E Kiltie, and Robert G Bristow. Targeting homologous recombination using imatinib results in enhanced tumor cell chemosensitivity and radiosensitivity. *Molecular cancer therapeutics*, 8(1): 203–213, 2009.

[55] Chaoyang Sun, Jun Yin, Yong Fang, Jian Chen, Kang Jin Jeong, Xiaohua Chen, Christopher P Vellano, Zhenlin Ju, Wei Zhao, Dong Zhang, et al. Brd4 inhibition is synthetic lethal with parp inhibitors through the induction of homologous recombination deficiency. *Cancer cell*, 33(3):401–416, 2018.

[56] Greta Bagnolini, Domenico Milano, Marcella Manerba, Fabrizio Schipani, Jose Antonio Ortega, Dario Gioia, Federico Falchi, Andrea Balboni, Fulvia Farabegoli, Francesca De Franco, et al. Synthetic lethality in pancreatic cancer: Discovery of a new rad51-brca2 small molecule disruptor that inhibits homologous recombination and synergizes with olaparib. *Journal of medicinal chemistry*, 63(5):2588–2619, 2020.

[57] Przemek M Krawczyk, Berina Eppink, Jeroen Essers, Jan Stap, Hans Rodermond, Hanny Odijk, Alex Zelensky, Chris van Bree, Lukas J Stalpers, Marrije R Buist, et al. Mild hyperthermia inhibits homologous recombination, induces brca2 degradation, and sensitizes cancer cells to poly (adp-ribose) polymerase-1 inhibition. *Proceedings of the National Academy of Sciences*, 108(24):9851–9856, 2011.

[58] WV Mayneord. The significance of the roentgen. *Acta Int Union Against Cancer*, 2:271, 1937.

[59] ML Taylor, RD Franich, JV Trapp, and PN Johnston. The effective atomic number of dosimetric gels. *Australasian Physics & Engineering Sciences in Medicine*, 31(2):131–138, 2008.

[60] ML Taylor, RL Smith, F Dossing, and RD Franich. Robust calculation of effective atomic numbers: The auto-zeff software. *Medical physics*, 39(4):1769–1778, 2012.

[61] ÖF Özpolat, B Alım, E Şakar, M Büyükyıldız, and M Kurudirek. Phy-x/zextra: a software for robust calculation of effective atomic numbers for photon, electron, proton, alpha particle, and carbon ion interactions. *Radiation and environmental biophysics*, 59(2):321–329, 2020.

[62] The International Commission on Radiological Protection (ICRP). Draft for consultation: Environmental protection. Important note by the authors: "Information contained in this document is preliminary and only for internal use by ICRP. It should, therefore, not be cited in any published material until final approval by ICRP.".

[63] Sasha Belenkov (PerkinElmer). Email correspondence. 3 October 2022.

[64] Freek Beekman Ruud M. Ramakers. Online meeting. 10 October 2022.

[65] Willi Kalender, Ben Durkee, Olievr Langner, Elizaveta Stepina, and Marek Karolczak. Comparative evaluation: acceptance testing and constancy testing for micro-ct scanners. *Biomed. Tech*, 50(2): 1192–1193, 2005.

[66] Vicki Trier Taasti, Ludvig Paul Muren, Kenneth Jensen, Jørgen Breede Baltzer Petersen, Jesper Thygesen, Anna Tietze, Cai Grau, and David Christoffer Hansen. Comparison of single and dual energy ct for stopping power determination in proton therapy of head and neck cancer. *Physics and Imaging in Radiation Oncology*, 6:14–19, 4 2018. ISSN 24056316. doi: 10.1016/j.phro.2018.04.002.

[67] Ernst van der Wal (DEMO). Email correspondence. 9 June 2022.

[68] Mitch Bartlett (Technipages). 3d printing material guide: What to know about hips. `https://www.technipages.com/3d-printing-material-guide-what-to-know-about-hips`, Accessed 10 October 2022.

[69] Kees Spruijt (Holland PTC). Meeting. 7 September 2022.

[70] M-C Vozenin, Jolyon H Hendry, and CL Limoli. Biological benefits of ultra-high dose rate flash radiotherapy: sleeping beauty awoken. *Clinical oncology*, 31(7):407–415, 2019.

[71] SR McKeown. Defining normoxia, physoxia and hypoxia in tumours—implications for treatment response. *The British journal of radiology*, 87(1035):20130676, 2014.

[72] Harry Towbin, Theophil Staehelin, and Julian Gordon. Electrophoretic transfer of proteins from polyacrylamide gels to nitrocellulose sheets: procedure and some applications. *Proceedings of the national academy of sciences*, 76(9):4350–4354, 1979.

[73] Michael T. Certo, Byoung Y. Ryu, James E. Annis, Mikhail Garibov, Jordan Jarjour, David J. Rawlings, and Andrew M. Scharenberg. Tracking genome engineering outcome at individual dna breakpoints. *Nature Methods*, 8:671–676, 8 2011. ISSN 15487091. doi: 10.1038/nmeth.1648.

A

Appendices

A.1. Molecular techniques

Western blot

Western blotting is a commonly used method to detect proteins, which relies on protein separation by size on a gel, the transfer to a membrane, and specific antibody binding to only visualise the protein of interest and was invented in 1979 by Towbin et al. [72]

First, the samples are loaded on a gel containing a dense mesh with a voltage applied along it. Due to the voltage, the proteins migrate through the gel towards the anode and their speed is determined by their size. To make sure that proteins are separated based on their length instead of the radius of their tertiary structure, samples are first supplemented with Laemmli buffer. The component sodium dodecyl sulfate (SDS) within this buffer denatures proteins and coats them with linear charges, ensuring migration through the gel independent of protein folding and inherent charges. This buffer furthermore contains glycerol which thickens the sample and tris which protects the peptide bonds from breaking.

Next, electroblotting is performed in which an assembly is made containing among others the gel and a membrane over which a voltage is applied. The negatively coated proteins in the gel are attracted toward the positive anode and bind to the non-permeable membrane.

The membrane is supplemented with a primary antibody binding specifically to the protein of interest. However, since the antibody can bind non-specifically to other proteins as well, the membrane is maintained in blocking buffer to prevent a homogeneous background signal. At last, the primary antibody is bound by a secondary antibody specifically, which is linked to horseradish peroxidase (HRP). During imaging, a chemiluminescent substrate (ECL) is added to the blot, this substrate is cleaved by the HRP enzyme leading to luminescence. Therefore, luminescence only occurs at the blot membrane where HRP and thus the specific protein are available.

Traffic Light Reporter assay

The traffic light reporter assay with flow cytometry is used for quantification of homologous recombination and non-homologous end-joining rates after induced double-stranded breaks. In flow cytometry cells flow through the flow cytometer one-by-one and hit by a laser. Fluorescently labeled cells absorb this light and emit light of another wavelength which is detected. The traffic light reporter assay is based on a construct and donor template as designed by Certo et al. [73] (see Fig. A.1). The construct contains a functionally enhanced GFP gene containing a nuclease target and an out-of-frame mCherry gene, and the separate donor template is a truncated GFP gene. Since the enhanced and truncated GFP genes and out-of-frame mCherry genes cannot be translated to functional proteins, cells without any DNA damage in the eGFP gene do not emit fluorescence.

The endonuclease I-SceI is supplemented and binds the nuclease target site in the eGFP gene leading to a double-stranded break. Upon repair using homologous recombination, the separate truncated gene is used as a donor template to repair the DSB in the enhanced GFP gene, resulting in a fully functional GFP gene. These green fluorescent cells can be sorted and collected by flow cytometry.

The double-stranded break could have been repaired via non-homologous end-joining as well. In this case, the damaged eGFP gene is ligated potentially leading to a frameshift. In approximately a third of the cells, this leads to an in-frame mCherry gene, due to which red fluorescence can be measured by flow cytometry.

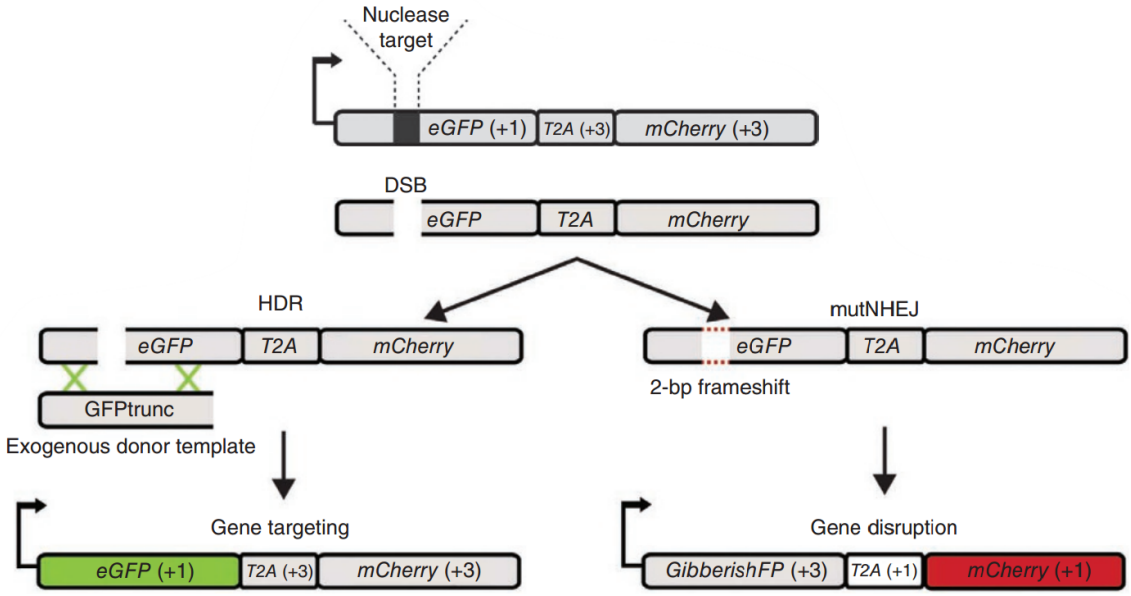

Figure A.1: **The traffic light reporter essay.** Binding of endonuclease I-SceI to the nuclease target site, results in a double-stranded break in the eGFP gene. Repair via homologous recombination makes use of an exogenous donor template with truncated GFP, leading to a functional GFP gene. Ligation of the eGFP gene via non-homologous end-joining may lead to a frameshift resulting in a functional mCherry gene. Via flow cytometry, detection of green and red fluorescence can be linked to homologous recombination and non-homologous end-joining rates after double-stranded breaks. Figure from Certo et al. [73]

A.2. Proton irradiation set-ups

	Proton with AZD7648	Proton with B02	Film calib	Phantom	Dose rates 1	Dose rates 2	Dose rates 3	FLASH 1	FLASH 2
Current (nA)	800	800			798	798	798	800	800
Energy (MeV)	150	150	150	150	150	150	150	250; 150	250; 150
Dose rate (Gy/min)	9.92	9.3			9.1; 1.5	10.68; 1.52	9.88; 1.66	4044; 9.66	5068; 6.08
Exit window Position (cm)	0	0	0	0	0	0	0	0	0
First foil Position (cm)	2.1	2.1	2.1	2.1	2.1	2.1	2.1	-	-
Beam monitor Position (cm)	14.5	14.5	14.5	14.5	14.5	14.5	14.5	14.5	14.5
Ring scatterer Position (cm)	52.0	52.0	52.0	52.0	52.0	52.0	52.0	52.0	52.0
Type	Thin	Thin	Thin	Thin	Thin; Thick	Thin; Thick	Thin; Thick	-; Thin	-; Thin
Ridge filter Position (cm)	91.0	91.0	91.0	91.0	91.0	91.0	91.0	45.0	45.0
Collimator Position (cm)	104.5	104.5	104.5	104.5	104.5	104.5	104.5	-	-
Hole (cmxcm)	10x10	10x10	10x10	2x2	10x10	10x10	10x10	-	-
Scattering foils Position (cm)	-	-	-	-	-	-	-	200.0	200.0
Collimator Position (cm)	173.5	173.5	173.5	173.5	173.5	173.5	173.5	230.5	230.5
Hole (cmxcm)	10x10	10x10	10x10	1x1	10x10	10x10	10x10	2.8x2.8	2.8x2.8
RW3 slabs Thickness (cm)	12.1	12.1	12.3	12.3	9,5; 5.0	12.1; 7.6	12.1; 7.6	29.0; 10.4	29.0; 10.3
Sample Subject	T25 flasks with 4 mL medium	T25 flasks with 4 mL medium	EBT3 film	Phantom	T25 flasks with 4 mL medium	T25 flasks with 4 mL medium	T25 flasks with 4 mL medium	Filled 24 well plate	Filled 24 well plate

Table A.1: **Specifics of all proton irradiations.** All distances are described from the exit window to the center of the component. The first foil is a plate of 0.34 mm thick led. The beam monitor is 6.7 cm thick, yet in TOPAS its water-equivalent thickness of 0.022 cm is used. The thin ring scattering has an inner lead circle of 5.5 mm in radius and 1.5 mm thick and an outer aluminum ring around of 100 mm in radius and 5.0 mm thick. Both brass collimators are 7.0 cm and the scattering foils are together 4.2 mm of led. The RW3 slabs are placed just behind the last collimator and the sample just behind the RW3 slabs. These three components are touching each other.

A.3. Full western blots

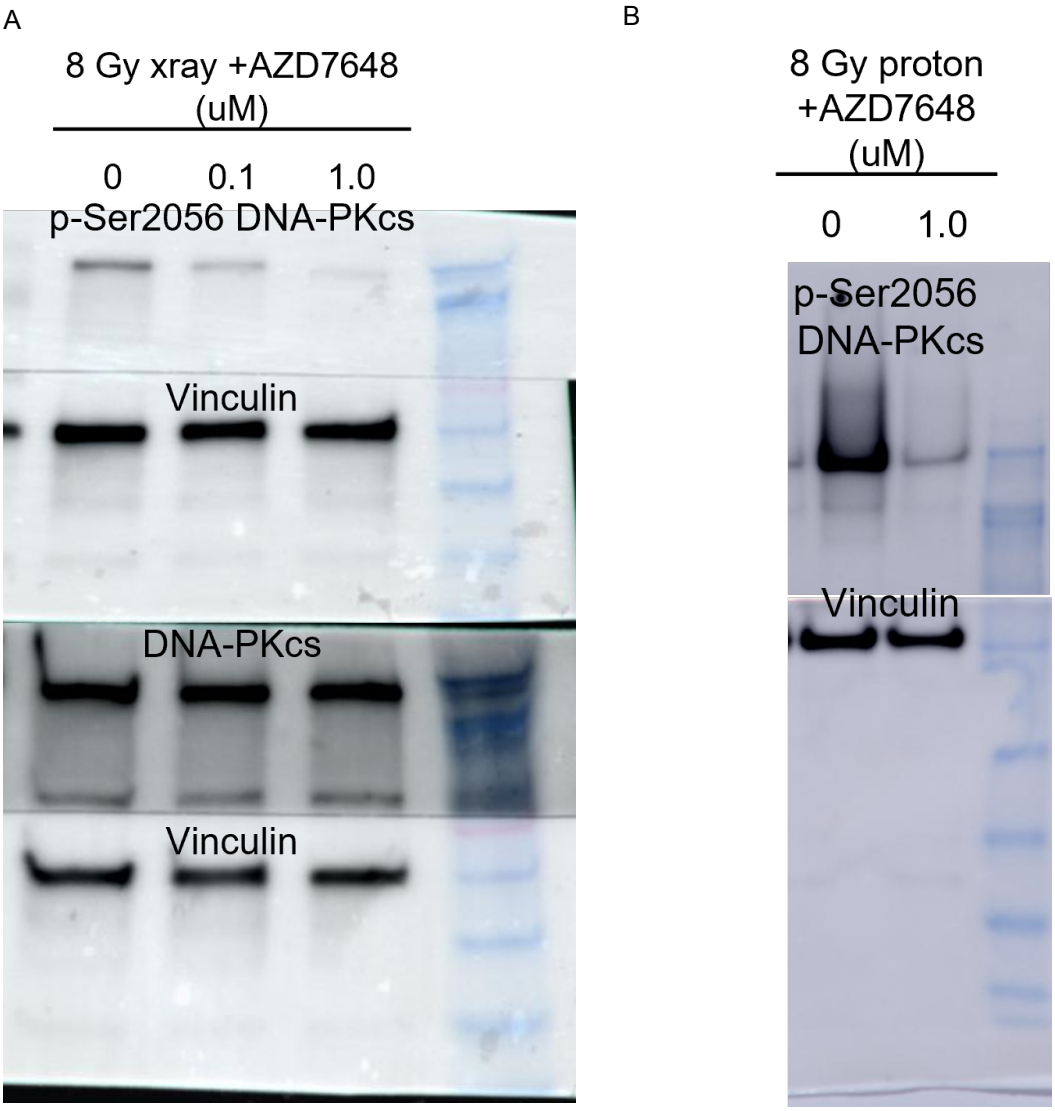

Figure A.2: **Complete western blots to validate p-Ser2056 DNA-PKcs inhibition during irradiations.** (A) Westernblot of p-Ser2056 DNA-PKcs inhibition by AZD7648 and total DNA-PKcs expression during x-ray irradiation (complete version of Fig. 3.1e). (B) Westernblot of p-Ser2056 DNA-PKcs inhibition by AZD7648 during proton irradiation (complete version of Fig. 3.1g). The ladders are HiMark Pre-stained Protein Standard (InVitrogen).

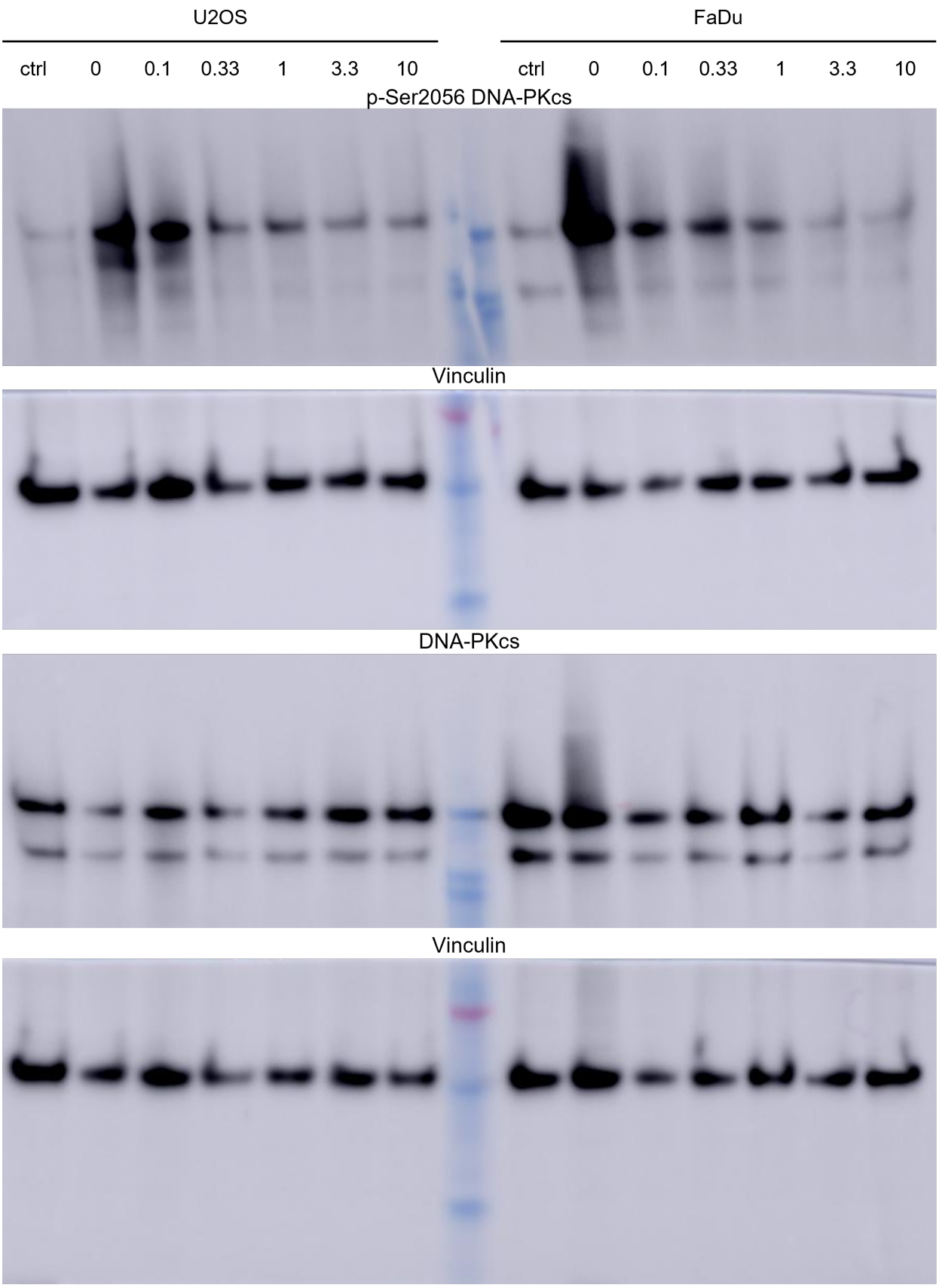

Figure A.3: **Complete western blots to assess p-Ser2056 DNA-PKcs inhibition by AZD7648.** Westernblot of p-Ser2056 DNA-PKcs inhibition by AZD7648 and total DNA-PKcs expression (complete version of Fig. 3.1b). The ladder is HiMark Pre-stained Protein Standard (InVitrogen).

A.4. Extra data

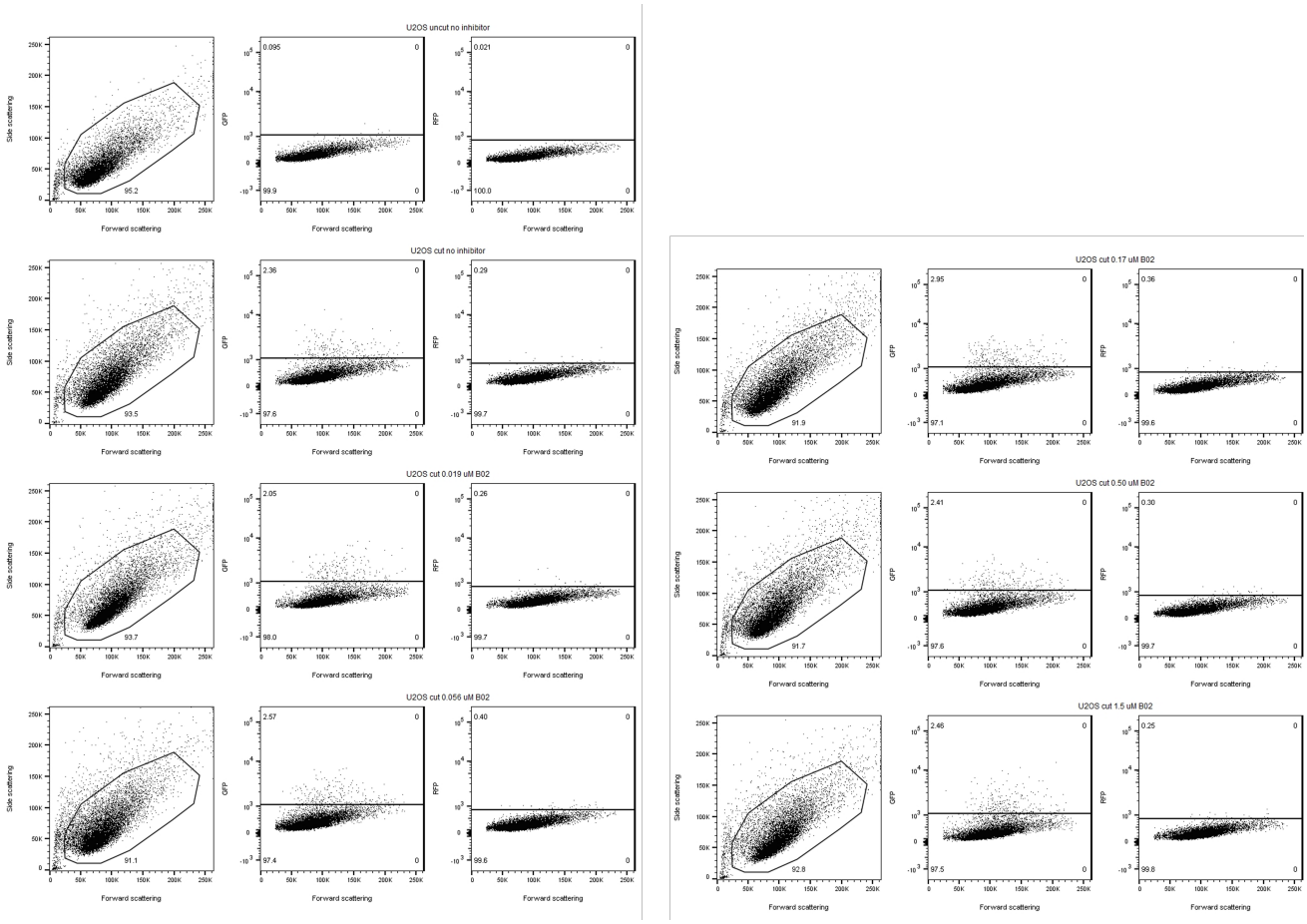

Figure A.4: **Complete flow-cytometry results for U2OS cells with B02 incubation.** For uncut and cut U2OS cells incubated with 0 until 1.5 µM B02, four graphs are shown. The gate in the forward vs side scattering graph selects alive single cells. In the forward scattering vs GFP or mCherry graphs, cells with GFP or mCherry signal exceeding the gate were denoted as GFP- or mCherry positive cells. In the GFP vs mCherry graph, any cells deviating from the diagonal express one of the fluorophores.

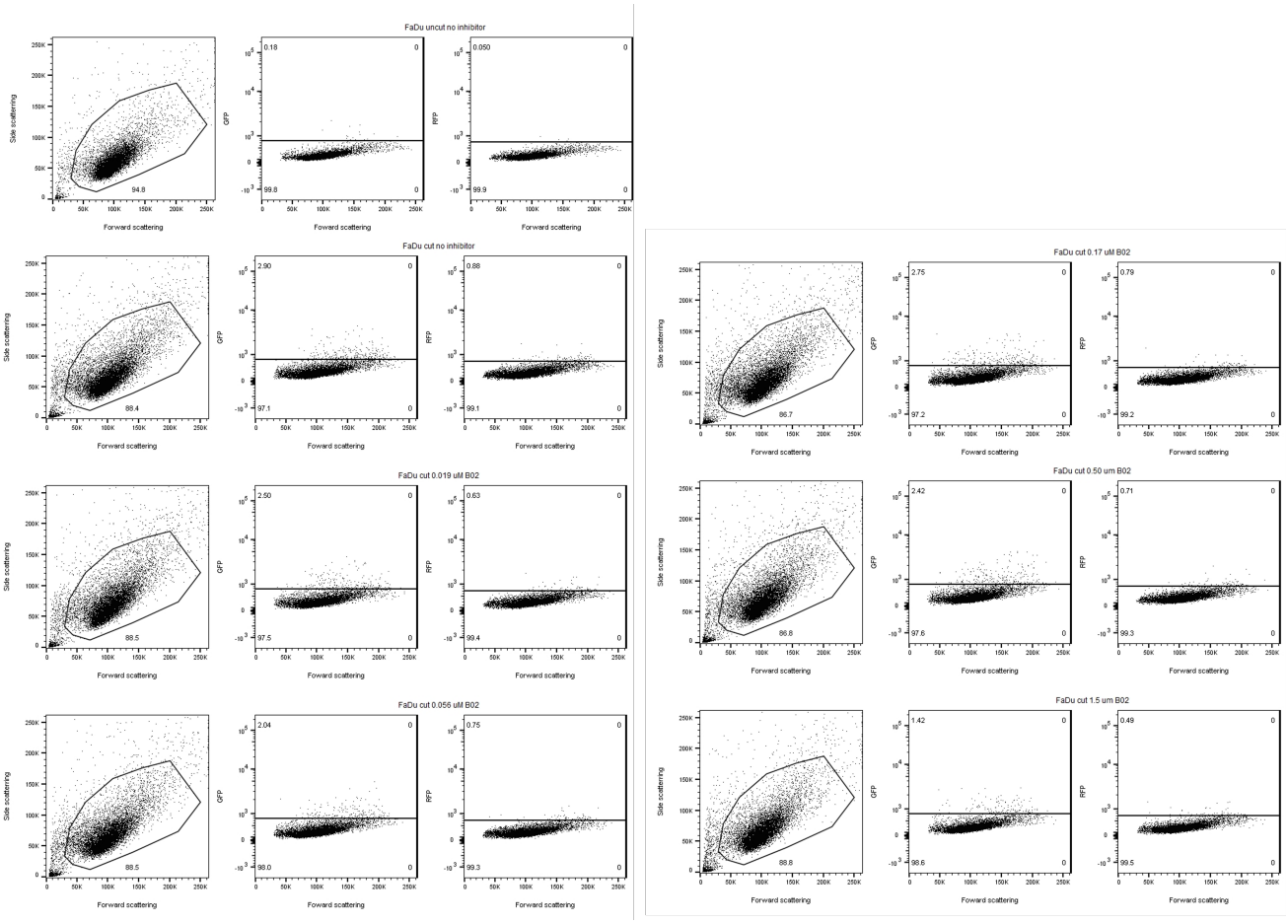

Figure A.5: **Complete flow-cytometry results for FaDu cells with B02 incubation.** For uncut and cut FaDu cells incubated with 0 until 1.5 µM B02, four graphs are shown. The gate in the forward vs side scattering graph selects alive single cells. In the forward scattering vs GFP or mCherry graphs, cells with GFP or mCherry signal exceeding the gate were denoted as GFP- or mCherry positive cells. In the GFP vs mCherry graph, any cells deviating from the diagonal express one of the fluorophores.

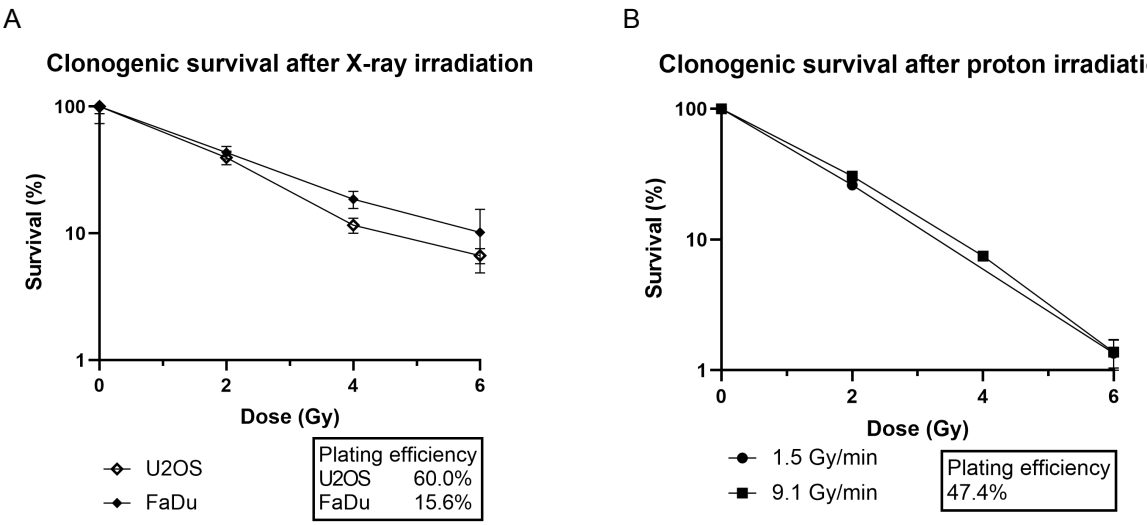

Figure A.6: **Extra clonogenic survival graphs after x-ray and proton irradiations.** (A) Clonogenic survival of U2OS and FaDu after x-ray irradiation (similar as results of Fig. 3.8a). (B) Clonogenic survival of FaDu after proton irradiations with two low dose rates. The cells were not exposed to medium during the irradiation.

Tissue	CT range (HU)		Elemental composition (%) H	C	N	O	Mg	P	Cl	Ar	Ca
Air	-1024	-950	0.00	0.00	75.50	23.20	0.00	0.00	0.00	1.30	0.00
Lung	-950	-205	10.30	10.50	3.10	75.90	0.00	0.20	0.00	0.00	0.00
Soft tissue	-205	-39	10.34	47.20	1.46	40.94	0.00	0.05	0.00	0.00	0.00
Mix soft tissue	-39	-65	10.34	13.08	2.89	73.48	0.00	0.18	0.00	0.00	0.02
Connective tissue	-65	155	9.40	20.70	6.20	63.70	0.00	0.00	0.00	0.00	0.00
Skeletal tissue	155	345	8.84	42.27	2.70	36.80	0.00	3.00	0.00	0.00	6.39
Skeletal tissue	345	535	7.94	37.83	2.95	38.01	0.00	4.21	0.00	0.00	9.07
Skeletal tissue	535	725	7.15	33.93	3.17	39.07	0.00	5.27	0.00	0.00	11.41
Skeletal tissue	725	915	6.45	30.49	3.36	40.01	0.00	6.21	0.00	0.00	13.48
Skeletal tissue	915	1105	5.82	27.42	3.53	40.85	0.00	7.05	0.00	0.00	15.33
Skeletal tissue	1105	1295	5.27	24.68	3.68	41.60	0.00	7.80	0.00	0.00	16.98
Skeletal tissue	1295	1485	4.76	22.21	3.82	42.27	0.00	8.47	0.00	0.00	18.46
Skeletal tissue	1485	1675	4.31	19.97	3.95	42.88	0.00	9.08	0.00	0.00	19.81
Skeletal tissue	1675	1865	3.89	17.93	4.06	43.44	0.00	9.64	0.00	0.00	21.04
Skeletal tissue	1865	2055	3.52	16.07	4.17	43.94	0.00	10.14	0.00	0.00	22.16
Skeletal tissue	2055	2245	3.17	14.37	4.26	44.41	0.00	10.61	0.00	0.00	23.18
Skeletal tissue	2245	2435	2.85	12.80	4.35	44.84	0.00	11.04	0.00	0.00	24.13
Skeletal tissue	2435	2625	2.56	11.35	4.43	45.23	0.00	11.43	0.00	0.00	25.00
Skeletal tissue	2625	2815	2.28	10.00	4.51	45.60	0.00	11.80	0.00	0.00	25.81
Skeletal tissue	2815	3005	2.03	8.75	4.58	45.94	0.00	12.14	0.00	0.00	26.56
Skeletal tissue	3005	3071	1.87	7.96	4.62	46.16	0.00	12.36	0.00	0.00	27.04

Table A.2: **CT value to elemental composition as determined from the calibration with Gammex scanned by QuantumGx2.**

Tissue	CT range (HU)		Elemental composition (%) H	C	N	O	Mg	P	Cl	Ar	Ca
Air	-1024	-950	0.00	0.00	75.50	23.20	0.00	0.00	0.00	1.30	0.00
Lung	-950	-210	10.30	10.50	3.10	75.90	0.00	0.20	0.00	0.00	0.00
Soft tissue	-210	-80	11.19	51.83	1.18	35.37	0.00	0.04	0.00	0.00	0.00
Soft tissue	-80	-41	10.71	32.62	2.34	53.76	0.00	0.09	0.00	0.00	0.00
Mix soft tissues	-41	-25	10.34	13.08	2.89	72.67	0.00	0.18	0.00	0.00	0.02
Connective tissue	-25	105	9.40	20.70	6.20	62.20	0.00	0.00	0.00	0.00	0.00
Skeletal tissue	105	355	9.69	46.47	2.46	35.22	0.00	1.85	0.00	0.00	3.87
Skeletal tissue	335	605	8.88	42.49	2.68	36.28	0.00	2.94	0.00	0.00	6.26
Skeletal tissue	605	855	8.16	38.93	2.88	37.24	0.00	3.91	0.00	0.00	8.41
Skeletal tissue	855	1105	7.51	35.72	3.06	38.09	0.00	4.79	0.00	0.00	10.34
Skeletal tissue	1105	1355	6.92	32.82	3.23	38.87	0.00	5.58	0.00	0.00	12.08
Skeletal tissue	1355	1605	6.38	30.18	3.38	39.57	0.00	6.30	0.00	0.00	13.67
Skeletal tissue	1605	1855	5.89	27.78	3.51	40.22	0.00	6.95	0.00	0.00	15.11
Skeletal tissue	1855	2105	5.45	25.57	3.63	40.81	0.00	7.55	0.00	0.00	16.44
Skeletal tissue	2105	2355	5.03	23.54	3.75	41.35	0.00	8.11	0.00	0.00	17.66
Skeletal tissue	2355	2605	4.65	21.67	3.85	41.85	0.00	8.62	0.00	0.00	18.79
Skeletal tissue	2605	2855	4.30	19.93	3.95	42.32	0.00	9.09	0.00	0.00	19.83
Skeletal tissue	2855	3071	3.99	18.43	4.04	42.72	0.00	9.50	0.00	0.00	20.74

Table A.3: **CT value to elemental composition as determined from the calibration with Gammex scanned by VECTor.**